2017-04-01

Weathering Sequence of Young Basalts: A Case Study from Kohala, Hawaii

Kimberly Francis Sowards
Brigham Young University

Weathering Sequence of Young Basalts: A Case Study from Kohala, Hawaii

Kimberly Francis Sowards

A thesis submitted to the faculty of
Brigham Young University
in partial fulfillment of the requirements for the degree of

Master of Science

Stephen Tracy Nelson, Chair
Barry R. Bickmore
John Henry McBride

Department of Geological Sciences

Brigham Young University

ABSTRACT

Weathering Sequence of Young Basalts: A Case Study from Kohala, Hawaii

Kimberly Francis Sowards
Department of Geological Sciences, BYU
Master of Science

Exposed weathering profiles of a series of Pololu lava flows in Kohala, Hawaii are ideal for investigating the sequence of reactions/reaction pathways of weathered basalt. Weathering reactions for saprolites show mineral sequences that include feldspar → halloysite ± gibbsite + solutes; clinopyroxene → hematite + minor halloysite + solutes; olivine → hematite + solutes; magnetite → hematite or other Fe-oxides/hydroxides. However, the presence of smectite in four samples suggests that smectite-group clays may form as short lived intermediates at the base of the weathering profile.

Regionally, on Kohala, soils and saprolites are dominated by halloysite with small quantities of other clays such as kaolinite, gibbsite, and smectite. However, one horizon in the weathering profile at the study site in Kohala is dominated by gibbsite. Smectite is found at the base of the profile above impermeable areas where mass leaching has left increased alkaline and alkaline earth elemental (Mg, Ca, Na, and K) abundances relative to the parent rock. The amount of elemental gain varies from -5% to +75% for samples with smectite.

Different climates generate different weathering profile depths. MASW (multi-channel analysis of surface waves) shows that the depth of the weathering profile is 15 meters. Seismic profiles correlate the depth of the weathering profile inland (~15 meters), with cliff face (~13 meters). Other than the gibbsite horizon, most mineral zones are too thin to be resolved through second-order velocity variations.

P-wave reflection surveys are unsuitable for imaging the base of the weathering front because the transition to fresh rock may be gradational. However, within the saprolite section, boundaries between relict lava flow textures produce reflections that mimic expected stratigraphic patterns. Perpendicular to the shoreline, reflectors dip gently seaward, whereas parallel to the shoreline, lenticular packages of relict lava flows are observed.

Keywords: Kohala, basalt, smectite, weathering, mass, leaching, rate, carbon dioxide

ACKNOWLEDGEMENTS

I would like to acknowledge those who have helped me with my thesis starting with faculty and staff, Kathryn Tucker and Kris Mortenson who have tirelessly answered questions and made sure everything was running smoothly. I would like to thank Dave Tingey, Kevin Ray, and John Yaede, who have helped me collect and analyze data. I also want to thank and acknowledge my committee members Steve Nelson, John McBride, and Barry Bickmore who have also been available answering questions, interpreting results, and coaching my writing. Finally, I want to acknowledge my husband Tyler who has been so supportive of me and has pushed me towards finishing.

TABLE OF CONTENTS

LIST OF FIGURES

LIST OF TABLES

1 INTRODUCTION

1.1 Background

It is well known that annual rainfall influences the thickness of laterite zones. When compared to older flows, younger lava flows produce shallower contacts between weathered and unweathered material in areas of equal precipitation. In the Hawaiian chain, the islands become younger from northwest to southeast (Fig. 1) (Frey et al., 1991). The Big Island has had less time to weather, and therefore has the thinnest and least extensive laterite zones of all the Hawaiian Islands.

The abundance and types of clay forming in the laterite zones depend on many variables including precipitation, age, composition, texture, climate, porosity, carbonate abundance, as well as other factors (Johnsson and Stallard, 1989; Bates, 1960; Barshad, 1957; Jackson, 1957). Bates (1960) observed that a mineral present as a transition phase in areas of high rainfall may be an end product in a more arid part of the island. On wet areas of the island, halloysite/kaolinite, and/or gibbsite dominate soils in terms of clay minerals.

Johnsson and Stallard (1989) noted that carbonate minerals can occur in soils where rainfall does not exceed 1000-2000 mm/yr. This could be a contributing factor in the formation of smectites due to the accumulation of Ca^{2+}. Capo et al. (2000) have discovered dolomite in the Kohala district of the Big Island of Hawaii, making it a likely area of Ca^{2+} and Mg^{2+} rich soil where smectite, a clay largely absent elsewhere, may be favored to form (Nelson et al., 2003; Chadwick et al., 2003; Hilley, 2010).

This and other studies have identified localized areas of smectite-rich soils (Nelson et al., 2013; Dessert et al., 2003; Chadwick et al., 2003; Johnsson et al., 1993; Johnsson et al., 1989). However, in most instances basalt ultimately weathers into Fe-oxides and kaolinite (Nelson et

al., 2003; Chadwick et al, 2003; Hilley, 2010). The presence of smectite in some locations, may indicate an intermediate phase of weathering before additional weathering produces halloysite/kaolinite.

The purpose of this study is to further understand the weathering process of basalts, specifically by capturing chemical weathering reactions in various stages of completeness in relatively young lavas. To accomplish this, we chose to investigate a cliff-face exposure on the north shore of the Kohala Peninsula where the degree of weathering is variable, the base of the weathering zone is exposed, and the basaltic substrate is relatively young (Chadwick et al., 2003; Sherrod et al., 2007).

1.2 Geologic Setting

As noted above, the islands of Hawaii become younger to the southeast (Fig. 1). This age transition is a result of volcanic activity as the Pacific plate moves over a stationary hotspot. The older islands of Nihau and Kauai are ~5 Ma, whereas the Big Island is still forming (Sherrod, 2007). Hotspot volcanic activity has created variably aged masses of fresh basalt.

Chemical weathering occurs everywhere, but at greatly different rates depending on rock type, temperature, and precipitation, among other variables. On the Big Island of Hawaii, many different rates of chemical weathering act on young basalt. The climate on the island varies drastically, ranging from rain forests > 6000 mm/year (windward) to deserts <250 mm/year (leeward) (Fig. 1). The windward side of the island weathers at a much faster rate largely because of dense vegetation. Heavily vegetated areas have high soil CO_2 concentrations because plants respire CO_2 through their roots. CO_2 concentrations are also enhanced by microbial activity (Berner, 2004). Precipitation dissolves soil CO_2, which produces acidic solutions that drive weathering reactions (Drever, 1994; Chadwick et al., 1994; Chadwick and Chorover, 2001;

Dessert et al., 2003; Nelson et al., 2013). The young bedrock of Kohala allows observation of chemical alterations in basalts in escarpments, road cuts, and wave-cut cliffs before deep, mature saprolite profiles are established. Often observed is the spheroidal weathering pattern as basalt weathers from the outside (Fig. 2). The ability to study chemical weathering in different climates over small spatial scales, and varying ages of mostly uniformed bedrock, makes the Big Island of Hawaii an excellent and unique natural laboratory to study the weathering sequence of young basalt.

The Kohala region of Hawaii is the oldest of five shield volcanos on the Big Island. It is composed of two series of flows, the Pololu and Hawi flows. The Pololu is the older series and ranges in age of 0.46 to 0.26 Ma, whereas the Hawi flows range from 0.23 to 0.12 Ma (Chadwick et al., 2003; Sherrod et al., 2007). The timing of the two flow sequences represents different stages in hot spot magmatism: shield stage (Pololu) and post-shield (Hawi). Pololu flows are tholeiitic, and Hawi flows are alkalic, ranging in composition from hawaiite to trachyte (Sherrod et al., 2007; Chadwick et al., 2003; Wolfe and Morris, 1996). Wave-cut cliffs in northern Kohala peninsula expose the Pololu flows.

Porder et al. (2007) studied the total mass loss and the rate of chemical weathering on three different flows on Hawaii. They were able to assess the significance of climate and substrate age in Hawaii. In this region, it is likely that the weathering rate of the basalt is between $\sim 24 \frac{ton}{km^2 yr}$ 0–10 ka to $< 2 \frac{ton}{km^2 yr}$ for older lava flows. Precipitation was determined to be a key factor in determining total mass loss. Chemical weathering also depends on tectonic uplift, erosion, climate, rock type, slope, or some combination of these (Porder et al., 2007; Nelson et al., 2013).

The study area is located on exposed Pololu material of wave-cut cliffs found in northern Kohala. This area receives ~2000 $\frac{mm}{year}$ of rain (Fig. 1). The cliff ranges in height of 14.6 m to 12.7 m (Fig. 3). The ground surface of the area is sloping seaward, specifically dipping to the north east. The cliff-face and immediately surrounding land is free of vegetation and shows evidence of mass wasting. Inland of the cliff, there are ~100 m of ironwood trees and grasses, adjacent to a fallow field. These conditions provided excellent access for geophysical surveys as well as rappel points for sample collection. The exposed cliff-face exhibits different stages of chemical weathering.

1.3 Significance

Basalt weathering has global and regional implications. The formation of soils and weathered rock is important for global climate studies and a basic understanding of the critical zone (Chadwick et al, 2003; Hilley, 2010). The thickness of the weathering profile is important for engineering purposes, since Hawaii has significant seismic hazard (Wong et al., 2011).

Globally, the long-term weathering process of basalts offers a sink for CO_2, effectively sequestering CO_2 from the atmosphere. Berner (1992), Drever et al. (1994), and Nelson et al. (2013), demonstrated this via chemical reactions by which this greenhouse gas is removed from the atmosphere. Even though more than four times as much CO_2 is stored in soils as in the atmosphere, the global impact of CO_2 related to weathering is not well understood (West, 2012; Hilley et al., 2010; Berner, 2004; Dessert et al., 2003; Chadwick et al., 2003; Chadwick et al., 1994; Rad et al., 2007). What separates the short-term CO_2 cycle from the long-term CO_2 cycle is the precipitation of CO_2 into rock, such as limestone. Chadwick et al. (1994) determined that in moist temperate grasslands the atmospheric net removal of carbon into the soils varied from $8.5\frac{g}{m^2yr}$ to $0.7\frac{g}{m^2yr}$. Chadwick et al. (1994) also discovered that as the soil ages, rates of carbon

sequestration increase from 2% to 8%. These weathering reactions are critical because they consume carbonic acid, generating bicarbonate in the process. This bicarbonate is transported by water into the oceans where it becomes buried as carbonate rock or organic-rich shale. Previous estimates of global CO_2 consumption by basalt are based on the current understanding of the basalt weathering process (Dessert et al., 2003; Navaree-Sitchle et al., 2007).

Additionally, the depth of the weathering profile is important in order to understand the weathering rate and thereby consumption of CO_2. On Earth's surface, the thickness of the weathering zone is poorly constrained (Berner, 2004). With the islands being relatively young, a great deal of variability in the thicknesses of weathering zones is preserved.

Multi-channel analysis of surface waves (MASW) is a geophysical tool that enables determining the depth of the weathering profiles where altered rock gives way to un-weathered lava as well as subsurface S-wave velocities. Strong motion stations located on the Big Island show shear-wave velocities ranging from ~276 to ~581 m/s (Wong et al., 2011). These velocities were measured at or near 22 different free field strong motion sites on the Big Island (Wong et al., 2011). These sites provided shear wave velocities for the upper 30 m, which is necessary for site-specific seismic hazard maps (Wong et al., 2011). For this study, changes in shear wave velocities were used to measure the depth of the weathering profile.

2 METHODS

To determine chemical weathering formulas from fresh to weathered rock, chemical and mineralogical analyses of basalt in different stages of alteration were obtained. In order to determine the depth of the weathering profile and physical characteristics of second order velocity variations, MASW experiments were collected in the field. All field and laboratory

analysis was conducted using Brigham Young University equipment and standard methodologies.

2.1 Field Methods

Initially, ten surface reference samples were collected throughout the Kohala peninsula including both Hawi and Pololu material (Fig. 4). The remaining field samples were collected by rappelling off the cliff faces (Fig. 3), as well as by sampling at the base of the cliff. Samples were collected systematically by identifying areas of different physical properties (texture, color, hardness, etc.) and then were prepared for lab analysis. Additional detailed analysis was conducted on remnant rock cores, R attached to sample name (e.g., Rap 1-2R) and their weathered rinds, S (e.g., Rap 1-2S). Additionally, a survey using standard methodologies was performed.

Geophysical surveys using MASW (both active-source and passive-source) and common-depth-point (CDP) P-wave reflection techniques were performed to determine the depth of the weathering profile as well as its internal structure. The origin of apparent second-order S-wave velocity variations were investigated, as well as relict internal flow structures. Features of seismic profiles were then related to cliff exposures. Data were collected along two profiles (Fig. 5).

The MASW methods used by Yaede et al. (2015) on the island of Oahu to study weathering of basalt lavas were also employed for active and passive MASW surveys for the study site. These methods were employed because interior, as well as the base of the weathered zone may be gradational and produce only diving waves but few or no reflections. However, it is possible that the base of the weathered zone, and relict flow fabrics within the weathered zones may produce reflections. Thus, CDP surveys were also conducted along each line. All geophones

used in the surveys had a resonant frequency of 4.5-Hz. MASW surveys were recorded with no field frequency filters. CPD surveys included a frequency field filter of 15-500 Hz. Data for the active surveys were recorded at 0.5-ms sample rate after striking a metal plate with a 5.4-kg hammer. The signal-to-noise ratio for the active-source surveys was improved by stacking the source (usually three strikes, summed in the field). The stacked CDP reflection sections were converted from time to depth based on the RMS velocity structure used to correct for normal move-out variation; however, due to the poor resolution of reflected energy, the accuracy of the depth conversion is limited.

2.2 Laboratory Methods

Major and minor elements were measured at BYU using a wavelength-dispersive X-ray fluorescence spectrometer (Rigaku Primus III instrument) on glass disks made with Li-metaborate flux using standard methods. Trace elements were measured from pressed powder pellets. Materials for both glass disks and powder pellets were calcined at 1000°C. Pressed powder pellets that were not heat treated outgassed water so that the instrument could not obtain sufficient vacuum. After analysis, the loss on ignition (LOI) was added back to the total and renormalized to 100%, in the case of major elements. Also, the effect of calcining on trace element concentrations was corrected by adjusting for the mass losses of volatiles. Because the cliff face receives sea spray, salt components were mathematically removed from major and minor element concentrations by assuming all Cl^- was derived from sea water (Kester et al., 1967).

Values for pH were measured by taking 100 ml of dry sample and filling the pore space with distilled water. The following mixture was then measured with a pH meter. Standard

solutions of pH 4, 7, and 10 were measured after each sample and an independent calibration was made for each sample.

All geochemical results were then compared using a correlation matrix. The significance of each correlation was calculated using a t-distribution (significant: p = 0.01-0.05, and highly significant: p < 0.01)

$$\tau_j = \frac{C_{j,w}C_{i,p}}{C_{j,p}C_{i,w}} - 1$$

Equation 1: from Brantley and White (2009) calculates a mass transfer value

Leaching and mass transfer indices Tau (τ) were calculated following the methods of Brantley and White (2009). τ represents the fraction of each element leached or accumulated by weathering, where C represents the concentration of a specific element or oxides. Concentrations are multiplied by the parent concentration (p), and the weathered material composition (w). The subscript (i) denotes a presumed immobile element, whereas (j) denotes all other elements. For samples from the study area, average compositions of samples with an LOI < 5% were used as the parent material. For reconnaissance samples taken from the top of Hawi flow, parent samples were obtained by averaging major element values of samples geographically near the sample location (Wolfe and Morris, 1996). Ti was assumed to be an immobile element

Samples were prepared for mineralogical analysis by X-ray diffraction using a Rigaku MiniFlex 600 X-ray diffractometer with Cu radiation followed by data reduction to semi-quantitative estimates of mineralogy using RockJock v. 11 (Eberl, 2008). Selected samples were analyzed to test for the presence of swelling clays by glycolation (Moore and Reynolds, 1997). Splits of all samples were treated with formamide using the methods of Churchman et al. (1984), and Theng et al. (1984) to discriminate halloysite from kaolinite.

Weathering formulas were created by modeling the crystallization of a parent composition in the program MELTS (Ghiosoro and Sack, 1995; Asimow and Ghiorso, 1998) to establish reactant phases. Calculations were conducted at 1 bar at the QFM buffer. Magma was allowed to crystalize close to 13% to approximate observed mean phenocryst abundances of other Hawaiian tholeiites (Haskins and Garcia, 2004). Starting composition for the groundmass was calculated by subtracting the composition of the phenocryst from the parent rock total formula, and allowing the following liquid composition (87% of total mass) to crystallize to completion at 1 bar at the QFM buffer. Reaction products were determined by X-ray diffraction.

3 RESULTS

First, geochemical results are discussed to properly interpret weathering patterns and clay formation, including ten reference samples that were collected around the Kohala region (Fig. 4). The cliff-face and the Kohala regional samples are compared side by side to determine (1) the role of climate and elemental leaching in regards to clay formation, and (2) to compare consistency in weathering behaviors throughout the region (Tables 1-13). Subsequently, geophysical results are presented from the CDP and MASW (active and passive) surveys.

3.1 Soil Chemistry

As minerals weather, ions are leached out and hydrolysis and oxidation reactions produce new phases. Leaching occurs at increasing intensities with increasing rainfall. However, rain amount and leaching intensity are not related by a simple linear relationship, rather there appear to be distinct step-wise thresholds (Chadwick et al., 2003). In northern Kohala, different climates, and different intensities of leaching exist. Figures 6, 7, 8, Tables 13 and 14 show τ values for samples collected at the same area, but at different depths. Figure 9, and Tables 13 and

14, show results from samples collected on Hawi and Pololu materials in areas of variable rainfall.

In all Kohala samples, elements Si, Mg, Ca, and Na have similarly high τ values of leaching, except four samples: Rap 1-9, Rap 2-6, Misc. 2, and Misc. 10, which experienced elemental gains in Si, Mg, Ca, and Na, and contain smectite. The presence of these four elements are positively correlated with pH at a highly significant level.

The degree of weathering is reflected in major element chemistry. In this environment, Si can be used as a proxy to track weathering (Nelson et al., 2012; Goodfellow et al., 2015; Brantley and White, 2009). Mobile ions such as Mg^{2+}, Ca^{2+}, and Na^{+}, reported as MgO, CaO, and Na_2O, show significant depletion from 10.18, 9.97, and 3.92 wt. % to as low as 0.53, 0.03, and 0.06 wt. %. However, less weathered samples near the base of the profile show less depletion (see Table 13 and Table 14).

Samples in low precipitation areas experienced little leaching of low field strength elements K and P compared to areas that experience high precipitation (Brantley and White, 2009). Ti does not show any mass loss or gain because this element was assumed to be immobile (Table 13, Table 14 and Equation 1).

3.2 Soil Mineralogy

Two representative X-ray diffraction patterns depicting weathered and fresh samples are presented in Figure 10. Weathered samples contain abundant Fe-Ti oxides (20 – 46 wt. %), and clays. Regionally, soils and saprolites are dominated by halloysite with small quantities of other clays such as kaolinite, gibbsite, and smectite. Exceptions include one horizon in the weathering profile that favored smectitie, and one horizon and location that favored gibbsite formation (Tables 1- 4). In contrast, unweathered samples contained 8 – 23 wt. % Fe-Ti oxides, including

ilmenite, and magnetite. These samples also contained anorthoclase (3 – 18 wt. %), plagioclase (2 – 55 wt. %), augite (6 – 26 wt. %), olivine (0.3 – 13.6 wt. %), and hypersthene (2 – 5 wt. %).

A few laterite samples (Rap 1-9, Rap 3-6, Misc. 2, and Misc. 10) show broad peaks at ~11 Å. generally indicative of the smectite group. When treated with ethylene glycol, 11-Å peaks are shifted to ~13 Å confirming the presence of smectites (Fig. 11) (Moore and Reynolds, 1997).

Initially, samples were dried at 60°C for XRD preparation. Oven drying caused the 10 Å (8° two theta) peak of halloysite to collapse to 7 Å (12° two theta). Since clay polymorphs kaolinite and dehydrated halloysite have peaks near 7 Å, semi-quantitative estimates of mineralogy did not resolve the presence of kaolinite versus halloysite very well. Treating samples with formamide causes the basal reflections in halloysite to expand to 10 Å allowing differentiation between the two clays (Churchman et al.; 1984, Theng et al., 1984). However, air-dried samples also had peaks around 10- Å instead of the 12 Å peak of oven-dried samples. While kaolinite is present in some samples, halloysite is the dominant clay, (Fig. 12). Halloysite was found to have a highly significant positive correlation with pH.

Oxide minerals such as magnetite, ilmenite, hematite, goethite, maghemite, ferrihydrite, and rutile were found in abundance depending on the degree of weathering. Goethite, and ferrihydrite were found to have a highly significant negative correlation with pH, whereas the other Fe-oxides had no significant correlation with pH. Less weathered samples contained more magnetite, while extremely weathered samples contained more goethite.

3.3 Seismic Data

Two geophysical lines were recorded, BIH Line 2 and BIH Line 3. Each line recorded both active and passive MASW, as well as CDP reflection profiles. BIH Line 2 is roughly

parallel to cliff face and shows lenticular packages of reflections, and BIH Line 3 is roughly perpendicular to the cliff face and shows seaward dipping reflections (Fig. 5). These profiles show shear wave velocity from the ground surface down to 35 m (Fig. 13). Like Yaede et al. (2015), 500 m/s is interpreted as the velocity of the boundary between saprolite and relatively unweathered basalt.

MASW for BIH Line 2 shows 2-D shear wave results (Fig. 13). BIH Line 3 covered a shorter distance, and therefore only a 1-D shear-wave profile was created from the active-source MASW (Fig. 13). Both lines show a general increase of velocity with depth from 200 to 1000 m/s, except for a velocity inversion at 5 m depth. This horizon at 5 m depth corresponds to a gibbsite-rich layer exposed in the cliff face (Fig. 13 and Fig. 14).

The CDP surveys were designed to image reflectors corresponding to possible impedance contrasts within the weathered zone using P-wave energy. This can be challenging due to the transitional character of physical properties within the weathered zone, which is more likely to show mostly diving waves, but few true reflections. This limitation means that most P-wave velocities derived from the CDP profiles are uncertain below 5 m depth. Despite these uncertainties, apparent reflections can be observed in the profile. The CDP profiles at BIH Line 2 and BIH Line 3 shows a horizon at the same depth as the velocity inversion found on the MASW results (Fig. 13).

A passive MASW surveys record a 1-D profile analyzing the shear wave velocity up to 30 m depth in profile BIH Line 3. The base of the weathering profile as seen on the survey, is found around 16 m. Due to the preferences of longer wavelengths in passive surveys, the velocity inversion of passive-source and active source results are off by ~2.5 m in the shallow

subsurface. However, both passive-source and active-source surveys correlate with depth showing the depth of the weathering profile to be consistent (Fig. 13).

4 DISCUSSION

4.1 Climatic Controls on Clay Formation

Minerals in Hawaiian volcanic rocks quickly weather into clays such as halloysite, kaolinite, gibbsite, smectite, as well as secondary Fe-oxides and hydroxides. The amount of each clay that forms depends on different environmental conditions (Joussein, 2016; Nelson, 2013; Chadwick et al., 2003; Hilley et al., 2010; Dessert et al., 2003; Johnsson et al., 1993; Dessert et al., 2003; Porder et al., 2007). Samples in the study area follow the following patterns, where hematite is used as a proxy for all Fe-oxides and hydroxides:

- feldspar → halloysite → gibbsite
- feldspar → smectite → halloysite
- feldspar → gibbsite
- clinopyroxene → halloysite + hematite → gibbsite + hematite
- olivine → hematite;
- magnetite → hematite.

The regional samples obtained within arid and humid soils of Pololu and Hawi materials exhibit different clay mineralogy's. Samples rich in halloysite are in areas that receive 1,000 – 2,500 mm of rain per year. Gibbsite dominates one arid soil that received 500 – 1,000 mm of rain per year (Fig. 4). It is important to note that smectite has both Al_2O_3 and MgO in the octahedral sheet, producing charge imbalances that require interlayer cations. However, for formula simplification it was assumed that Al_2O_3 is alone in the octahedral sheet.

Climate and precipitation are not the only conditions that affect the weathering of rocks. In Hawaii, vegetation abundance is a function of rainfall. As mentioned above, plants increase the amount of soil CO_2, reflected in carbonic acid production and producing an increased rate of weathering.

4.1.1 Phenocryst weathering

(1) Olivine weathering $200\ (Mg_{0.75}Fe_{0.25})_2Si_{200}O_{800} + 60800\ H^+ + 27\ O_2 = 50\ Fe_2O_3$ (hematite)$+ 200\ SiO_2 + 400\ Mn^{2+} + 29600\ Mg^{2+} + 400\ Ca^{2+} + 304\ H_2O$

(2) Feldspar weathering $100\ Na_{0.36}Ca_{0.64}Al_{1.63}Si_{2.37}O_8 + 163\ H_2O + 16300\ H^+ = 163\ Al(OH)_3$ (gibbsite) $+ 3600\ Na^+ + 100\ K^+ + 6300\ Ca^{2+} + 237\ SiO_2$

(3) Feldspar weathering $200\ Na_{0.36}Ca_{0.64}Al_{1.63}Si_{2.37}O_8 + 32600\ H^+ + 459\ H_2O = 163\ Al_2Si_2O_5(OH)_4$ (halloysite) $+ 148\ H_4SiO_4 + 7200\ Na^+ + 12600\ Ca^{2+} + 200\ K^+$

(4) Feldspar weathering $200\ Na_{0.36}Ca_{0.64}Al_{1.63}Si_{2.37}O_8 + 32600\ H^+ + 178\ SiO_2 = 163\ Al_2Si_4O_{10}(OH)_2$ (montmorillonite) $+ 7200\ Na^+ + 200\ K^+ + 12600\ Ca^{2+}$

4.1.2 Matrix weathering

(5) Olivine weathering $100\ (Mg_{0.30}\ Fe_{0.56}\ Mn_{0.14})_2\ SiO_4 + 18000\ H^+ + 29\ O_2 = 56\ Fe_2O_3$ (hematite) $+ 100\ SiO_2 + 2800\ Mn^{2+} + 6000 Mg^{2+} + 200\ Ca^{2+} + 90\ H_2O$

(6) Feldspar weathering $100\ Na_{0.50}\ Ca_{0.50}\ Al_{1.43}\ Si_{2.57}\ O_8 + 143\ H_2O + 14300\ H^+ = 143\ Al(OH)_3$ (gibbsite)$+ 5000\ Na^+ + 700\ K^+ + 4300\ Ca^{2+} + 257\ SiO_2$

(7) Feldspar weathering $200\ Na_{0.50}\ Ca_{0.50}\ Al_{1.43}\ Si_{2.57}\ O_8 + 28600\ H^+ + 599\ H_2O = 143\ Al_2Si_2O_5(OH)_4$ (halloysite) $+ 228\ H_4SiO_4 + 10000\ Na^+ + 8600\ Ca^{2+} + 1400\ K^+$

(8) Feldspar weathering $200\ Na_{0.50}\ Ca_{0.50}\ Al_{1.43}\ Si_{2.57}\ O_8 + 28600\ H^+ + 58\ SiO_2 = 143\ Al_2Si_4O_{10}(OH)_2$ (montmorillonite) $+ 10000\ Na^+ + 1400\ K^+ + 8600\ Ca^{2+}$

(9) Smectite weathering $Al_2Si_4O_{10}(OH)_2$ (montmorillonite) $+ H_2O =$

$Al_2Si_2O_5(OH)_4$ (halloysite) + 2 Si_2O

(10) Halloysite weathering $Al_2Si_2O_5(OH)_4 + H_2O = 2\ Al(OH)_3$ (gibbsite) + 2 SiO_2

(11) Magnetite weathering 300 $Fe_{1.41}\ Mg_{0.19}\ Fe_{0.71}\ Al_{0.09}\ Ti_{0.60}$ + 454 H_2O + -82700 H^+ + 94100 O^+ = 318 Fe_2O_3 (hematite)+ 180 TiO_2 + 5700 Mg^{2+}+ 27 Al $(OH)_3$ (gibbsite)

(12) Ilmenite Oxide weathering 2000400 $Mn_{0.05}Fe_{0.80}Mg_{0.05}Fe_{0.20}Ti_{0.90}O_3$ + 44008800 H^+ = 970194 Fe_2O_3 (hematite) + 182 $Ti_{10}O_2$ + 14002800 Mg^{2+} + 8001600Mn^{2+} + 220044 H_2O + 1435287 O_2

(13) Clinopyroxene weathering 200 $Ca_{0.19}Fe_{0.89}Mg_{0.86}Fe_{0.03}Al_{0.08}Si_{1.94}O_6$ + 42000 H^+ + 43 O_2 = 92 Fe_2O_3 (hematite)+ 372 SiO_2 + 8$Al_2Si_2O_5(OH)_4$ (halloysite) + 3800 Ca^{2+} + 17200 Mg^{2+} + 194 H_2O

(14) Clinopyroxene weathering 200 $Ca_{0.80}Fe_{0.45}Mg_{0.5}\ Fe_{0.05}Al_{0.15}Si_{2.0}\ O_6$ + 58000 H^+ + 22 O_2 = 49 Fe_2O_3 (hematite) + 354 SiO_2 + 13$Al_2Si_2O_5(OH)_4$ (halloysite) + 15800 Ca^{2+} + 13000 Mg^{2+} + 4 TiO_2 + 400 Na^+ + 264 H_2O

4.2 Clay Formation in a Weathering Profile

Clay formation in the weathering profile is controlled by depth, porosity, surface area, and water availability. Figure 12 presents a model for clay abundances in different horizons. Halloysite is the dominant clay present in the weathering sequence.

Reflectors interpreted on the BIH Line 2 and BIH Line 3 CDP profiles suggest contrasts in acoustic impedance (shear modulus or bulk density). In different volcanic flows, such as aa' and pahoehoe, different porosities are expected. These porosities (lower in aa' and higher in pahoehoe) influence the bulk density of the flow in the series. Reflections could be the result of different relict fabrics preserved in saprolite. Even though it is difficult to directly correlate these

contrasts to features observed in the cliff-face, they do suggest boundaries across which porosity and mineralogical content varies.

Gibbsite is found within a horizon at ~5 m depth. A few samples (Rap 1-2R, Rap 1-2S, Rap 1-3, Rap 2-3, Rap 2-4, Rap 3-2, Rap 3-3, and 202433 E) show relatively high abundances of gibbsite (Fig. 14 and Table 1-5). This horizon correlates with the velocity inversion on the MASW results and possibly to the prominent shallow reflector on the CDP profiles (Fig. 13).

Sample 202433 E located on the northern most tip of Kohala is the only surficial data point that contains a relatively high abundance of gibbsite. This sample of a Pololu material was measured in a different climate that receives less rain than the study area (Fig. 4). As discussed by Bates (1960), water has an important impact on the formation of gibbsite. Bates (1960) stated that there are three steps in the formation of gibbsite. First, is the removal of Si from halloysite. Next, is the dehydration of the Al-gel. Finally, as it dehydrates, gibbsite precipitates from solution. The velocity inversion near 5 m depth implies that different densities (or porosities) and/or shear moduli exist in the shallow subsurface. In low velocities zones where the gibbsite horizon occurs, it is likely that high porosity has resulted from strong leaching. If the halloysite had been leached and was dry enough, then the Al-gel dehydrates. This inversion could be indicative of a different flow from the Pololu series where weathering occurred before the next flow was deposited.

Swelling clays are located horizons that shows enrichment of τ values at about 10 m depth (Fig. 14). Typically, samples containing smectites were found near the base of the profile, and along the rim of weathering core stones. According to Galan (2006) and Bates (1960), smectite is commonly found at the lower part of the weathering profile when the profile is developed under high rainfall. Bates (1960) stated that smectite and halloysite often form at the

top of cliff-faces as olivine breaks down. The weathered remains of olivine move downward through cracks and fractures in the rocks each time there is precipitation. Galan (2006) and Bates (1960) noted that clay development is based on many factors and suggested that smectite formation occurs when conditions include base-rich parent rocks, poor drainage, low-lying topography, high pH, high silica activity, and an abundance of basic cations. Like Galan (2006) predicted, samples containing smectite have higher pH than other samples, higher silica abundance, and higher concentrations of alkaline, and alkaline earth elements (Table 13 and Table 14). There could be two reasons why samples at this horizon are relatively enriched: (1) samples at this location have recently begun the weathering process and have not been depleted yet; (2) leached ions from higher horizons have collected at the fresh rock-sea water interface. Since sea salts have been subtracted from samples, the ionic enrichments are not due to sea water.

Contrarily, this portion of the island receives relatively low annual rainfall, around 2,000-2,750 mm, and is not part of low-lying topography (Giambelluca et al., 2013). Smectite must be an early intermediate phase that briefly occurs early at the beginning of weathering process near the saprolite/bedrock contact. This boundary likely migrates downward with the weathering front.

4.3 Climate and Weathering Rates

Due to wave erosion, the cliff face is eroding by 0.8 mm per year. Values were obtained by a precision elevation survey of the ground surface, which show nearly the same slope in the slope of shallow reflections the seismic data. The ground covered by BIH Line 3 extends for 100 m inland and has a 5.72 m drop in elevation seaward (Fig. 13). On average, there is a 5.7% grade until it reaches the cliff-face. Starting approximately 16.72 m above sea level and assuming a

constant grade of 5.7%, at 0.36 Ma (Chadwick et al., 2003; Sherrod et al., 2007) the ground extended 292 m towards the sea, which translates to a landward erosion rate of 0.8mm per year.

Although the island is eroding due to physical abrasion along stream valleys, it is also eroding due to dissolution by ground and surface water. Near sea level, τ values show an average of 25% silica removed. By contrast, laterite samples at the top of the cliff-face show an average of 58% silica removed (Fig. 15). Although smectite bearing samples have positive τ values, they are the minority, and only slightly affect the averages. (Fig. 15).

For long time scales, the weathering of basalt acts as a sink for CO_2. Using the chemical equations (found above):

- feldspar → halloysite
- feldspar → smectite → halloysite

The same amount of CO_2 is consumed. Whether the end product is halloysite/kaolinite or gibbsite, the product clay assemblage has no effect on CO_2 consumption.

CONCLUSIONS

Northern Kohala provides an excellent natural laboratory to conduct weathering research. In this study, northern Kohala permitted the examination of systematic changes in the weathering profile with depth under the constraint of a uniform climate. Overall, leaching of mobile elements decreases from the surface down toward the interface between bedrock and saprolite. However, at 5 m depth there is a gibbsite-rich horizon that exhibits the greatest leaching. This likely reflects a relict horizon with greater initial permeability that diverted lateral flow through the weathering volcanic sequence. Thus, primary igneous textures can exert considerable control on the degree of weathering. Alternatively, this horizon could represent a paleosol. Toward the base of the weathering profile, including the rinds of some core stones, positive τ indices for Si,

Mg, Ca, and Na indicate accumulation of downward leaching elements within smectite-group clays. However, beside the basal location, the general lack of swelling clays suggest that they are minor, short-lived intermediate weathering products.

CDP profiles suggest that although the saprolite-bedrock contact may be transitional, relict igneous textures and features, such as volcanic fabrics and flow directions, are preserved in saprolite which provide impedance contrasts sufficient to produce reflections. However, due poorly resolved P-wave velocity control below 5 m, time-to-depth conversion is uncertain, making direct correlation difficult between the CDP profiles and cliff outcrop. The CDP profile parallel to the cliff face shows lenticular packages of reflections, as would be expected if the lava flowed seaward. Similarly, the CDP profile that is perpendicular to the cliff face shows seaward dipping reflections. Although imperfect, the base of saprolite horizon corresponds fairly well to the 500 m/s limit on the MASW S-wave velocity profiles. The MASW sections exhibit velocity inversions that correlate to the gibbsite-rich horizon in the cliff. This implies, by contrast, that significant second order velocity inversions, in terms of thickness, depth, and velocity contrast seen elsewhere in thick saprolite horizons (e.g., Yaede et al., 2015) may reflect significant mineralogical changes in the subsurface.

It is important to remember limitations of extrapolation. As has been seen above, rain amount, and density can have a significant result on the type of clays produced. The cliff-face is weathering quickly by waves, demonstrating that all minerals present have likely formed before being in contact with seawater.

REFERENCES

Asimow, P. D. and Ghiorso, M. S., 1998, Algorithmic modifications extending MELTS to calculate subsolidus phase relations: Mineral, v. 83, p. 1127–1132.

Bates, T., 1960, Halloysite and gibbsite formation in Hawaii: Clays and Clay Minerals, v. 9, p. 315-328.

Barshad, I., 1957, Factors affecting clay formation, California: The Clay Mineral Society, v. 6, p. 110-132 .

Berner, R. A., 1992, Weathering, plants, and the long term carbon cycle: Geochimica et Cosmochim. Acta, v. 56, p. 3225-323.

Berner, R.A., 2004, The Phanerozoic carbon cycle: CO_2 and O_2: New York, New York, Oxford University Press, pp. 158.

Brantley S. L. and White A. F., 2009, Approaches to modeling weathered regolith: Mineral Geochemistry v. 70, p. 435–484.

Capo, R. C., Whipkey, C. E., Blachere, J. R., Chadwick, O. A., 2000, Pedogenic origin of dolomite in a basaltic weathering profile, Kohala peninsula, Hawaii: Geology, v. 28, p. 271-274.

Chadwick, O. A., and Chorover, J., 2001, The chemistry of pedogenic thresholds: Geoderma, v. 100, p. 321-353.

Chadwick, O.A.,Gavendab, R.T., Kelly, E.F., Zieglera, K., Olsond, C.G., Elliotte, W.C., Hendricks, D.M., 2003, The impact of climate on the biogeochemical functioning of volcanic soils: Chemical Geology, v. 202, p. 195-223.

Chadwick, O. A., Kelly, E. F., Merritts, D. M., Amundson, R. G., 1994, Carbon dioxide consumption during soil development: Biogeochemistry, Vol 24, p. 115 – 127.

Churchman, G. J., Whitton, J. S., Claridge, G. G., Theng, B. K. G., 1984, Intercalation method using formamaide for differentiating halloysite from kaolinite: Clays and Clay Minerals, v. 32, p. 241-248.

Deer, H., Howie, R. Zussman, J., 1975, An Introduction to the Rock Forming Minerals, Longman Group Limited, London. Print.

Dessert, C., Dupréa, B., Gaillardet, J., François, L.M., and Allègreb, C.J., 2003, Basalt weathering laws and the impact of basalt weathering on the global carbon cycle: Chemical Geology, v. 202, p. 257-273.

Drever, J.I., 1994, The effect of land plants on weathering rates of silicate minerals: Geochimica. et Cosmochim, v. 58, p. 2325– 2332.

Dong, H., Jaisi, D.P., Kim, J., and Zhang, G., 2009, Microbe-clay mineral interactions: American Minerologists, v. 94, p. 1505-1519.

Eberl, D.D., 2008, User's guide to rockjoc – a program for determing quantitative mineralogy from powder x-ray diffraction data: Boulder, Colorado, USGS, p. 47.

Frey, F.A., Garcia, M.O., Wise, W.S., Kennedy, A., Gurriet, P., and Alberede, F., 1991, The evolution of Mauna Kea Volcano, Hawaii: Petrogenesis of tholeiitic and alkalic basalts: Journal of Geophysical Research, v. 96, p. 14347-14375.

Galan, E., 2006, Genesis of clay minerals: Handbook of Clay Science, Ch. 14, pp. 1129-1162

Giambelluca, T.W., Q. Chen, A.G. Frazier, J.P. Price, Y.-L. Chen, P.-S. Chu, J.K. Eischeid, D.M. Delparte, 2013: Online Rainfall Atlas of Hawai'i: Bull. Meteor. Soc 94, 313-316.

Ghiorso, M. S., and Sack, R. O., 1995, Chemical mass transfer in magmatic processes IV. A revised and internally consistent thermodynamic model for the interpolation and

extrapolation of liquid–solid equilibria in magmatic systems at elevated temperatures and pressures: Contributions to Mineralogy and Petrology, v. 119, p. 197–212.
Goodfellow, B. W., Chadwick, O. A., Hilley, G. E., 2013, Depth and character of rock weathering across a basaltic-hosted climosequence on Hawai'i: Earth Surface Processes and Landforms, vol. 39, p. 381-398.
Haskins, E. H., and Garcia, M. O., 2004, Scientific drilling reveals geochemical heterogeneity within the Ko'olau shield, Hawai'I. Contributions to Mineralogy and Petrolology, v. 147, p. 162–188.
Hilley, G.E., Chamberlain, C.P., Moon, S., Porder S., Willet, S.D., 2010, Competition between erosion and reaction kinetics in controlling silicate-weathering rates: Earth and Planetary Science Letters, v. 293, p. 191-199.
Jackson, M. L., 1957, Frequency distribution of clay minerals in major great soil groups as related to the factors of soil formation, California: The Clay Mineral Society, v. 6 p. 133-143.
Jones R. C., Babcock C. J., Knowlton W. B., 2000, Estimation of the total amorphous content of Hawai'i soils by the Rietveld method: Soil Sci. Soc. Am. J., v. 64, p. 1100–1108.
Johnsson M. J., Ellen S. D., McKittrick M. A., (1993) Intensity and duration of chemical weathering: an example from soilclays of the southeastern Koolau mountains, Oahu, Hawaii: Spec. Pap. – Geologic Society. of America. 284, 147–170.
Johnsson, M. J., and Stallard, R. F., 1989, Physiographic controls on the composition of sediments derived from volcanic and sedimentary terrains on Barro Colorado Island, Panama, AAPG Database, v. 59, p. 768-781.
Joussein, E., 2016, Geology and mineralogy of nanosized tubular halloysite, Developments in Clay Science, v. 7, p. 12-48.
Kester, D. R., Duedall, I. W., Connors, D. N., Pytkowicz, R. M., 1967, Preparation of artificial seawater, Limnology and Oceanography, v. 12, p. 176–179.
McDougall, I., and Swanson, D. A.; 1972, Potassium-argon ages of lavas from the Hawi and Pololu volcanic series, Kohala volcano, Hawaii: Geologic Society of America Bulletin, v. 83, p. 3731-3738.
Moore, D. M., and Reynolds, R. C., 1997, X-ray diffraction and the identification and analysis of clay minerals: Oxford University Press, New York. Edition 2, Print.
Nelson, S.T., Tingey, D.G., Selck, B., 2013, The denudation of ocean islands by ground and surface waters: The effects of climate, soil thickness, and water contact times on Oahu, Hawaii: Geochimica et Cosmochimica Acta, v. 103, p. 276-294.
Navarre-Sitchlera, A., and Susan Brantley, S., 2007, Basalt weathering across scales: Earth and Planetary Science Letters, v. 261, p. 321-334.
Porder, S., Hilley, G., Chadwick, O.A., 2007, Chemical weathering, mass loss, and dust inputs across a climate by time matrix in the Hawaiian Islands: Earth and Planetary Science Letters, v. 258, p. 414-427.
Rad, S. D., Allegre, C. J., Louvat, P., 2007, Hidden erosion on volcanic islands: ScienceDirect, v. 262, p. 109-124.
Sherrod D. R., Sinton J. M., Watkins S. E., Brunt K. M., 2007, Geologic map of the state of Hawai'i: OF 2007-1089, p. 85.
Theng, B. K. G., Churchman, G. J., Whitton, J. S., Claridge, G. G. C., 1984, Comparison of intercalation methods for differentiating halloysite from kaolinite, Clays and Clay Minerals, v. 32, p. 249-258.

Torrent, J., Benayas, J., 1977, Origin of gibbsite in a weathering profile from granite in west-central Spain: Geoderma, v. 19, p. 37-49.
West, J.A., 2012, Thickness of the chemical weathering zone and implications for erosional and climatic drivers of weathering and for carbon-cycle feedbacks: Geology, v. 40, p. 811-814.
Wolfe, E. W., and Morris, J., 1996, Sample data for the geologic map of the island of Hawaii: US Geologic Survey, IMAP, 2524.
Wong, G.I., Kenneth, H., Stoke, I., Cox, B.R., Yuan, J., Knudsen, K.L., Terra, F., Okubo, P., Yin-Cheng, L., 2011, Shear-wave velocity characterization of the USGS Hawaiian Strong-Motion Network on the island of Hawaii and development of an NEHRP site-class map: Bulletin of the Seismological Society of America, v. 101, p. 2252-2269.
Yaede, J.R., McBride, J.H., Nelson, S.T., Park, C.B., Flores, J.A., Turnbull, S.J., Tingey, D.G., Jacobsen, R.T., Dong, C.D., Gardner, N.L., 2015, A geophysical strategy for measuring the thickness of the critical zone developed over basalt lavas: Geosphere, v. 11, p. 513-532.

FIGURES

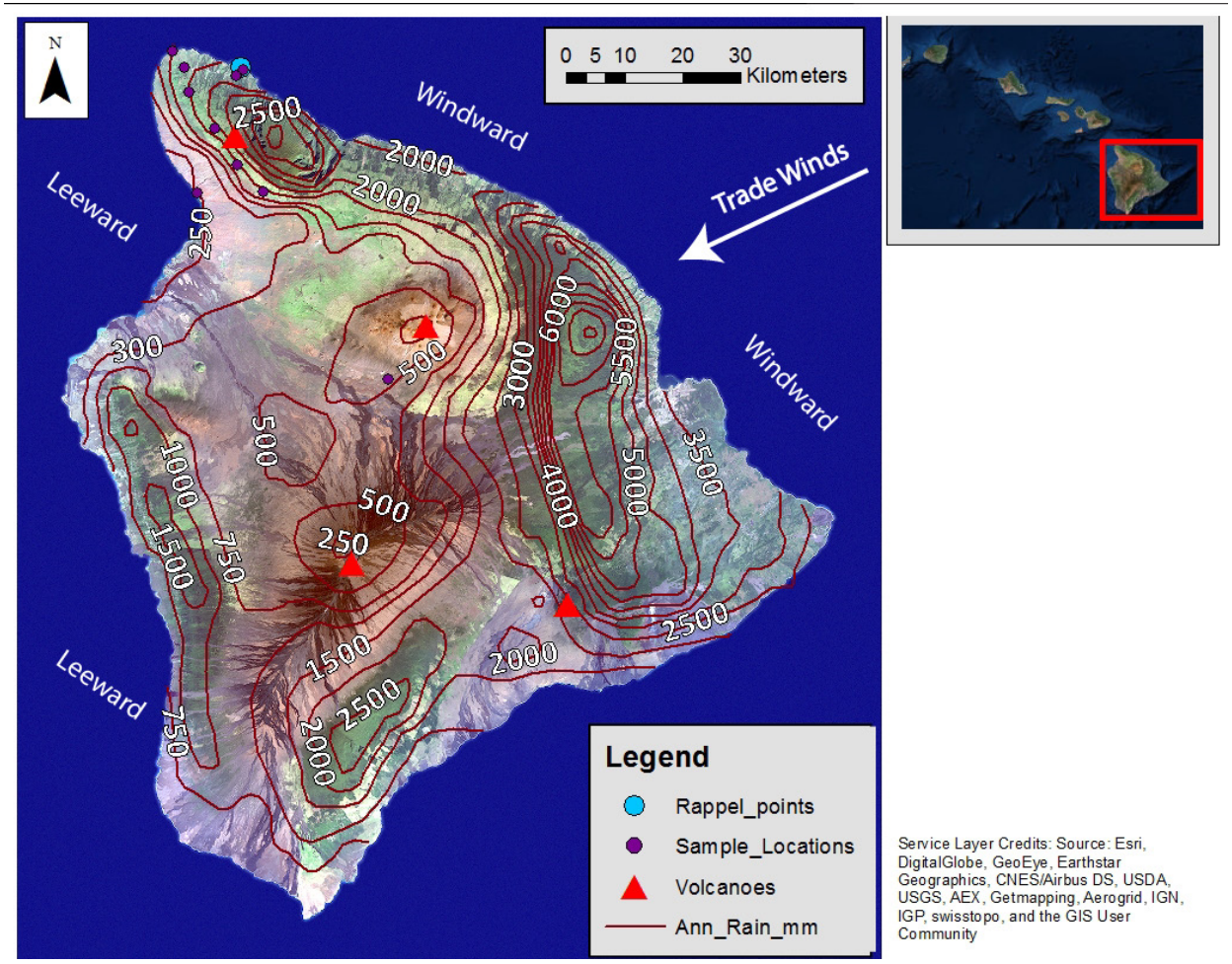

Figure 1: Landsat image of the Big Island with rain contours showing annual rain in mm (Giambelluca et al., 2013). Green areas are vegetated, dark brown represents fresh lava flows, and pink represents arid land. The concentration of vegetation on the windward side of the island compared to the leeward side of the island demonstrates the orographic effects of Mauna Loa and especially Mauna Kea.

Figure 2: Photograph looking down at the ground surface of columnar jointing visible in the weathering profile. As water seeped into the joints, the basalt column weathered from the outside in, leaving a weathering rind surrounding relatively fresh basalt.

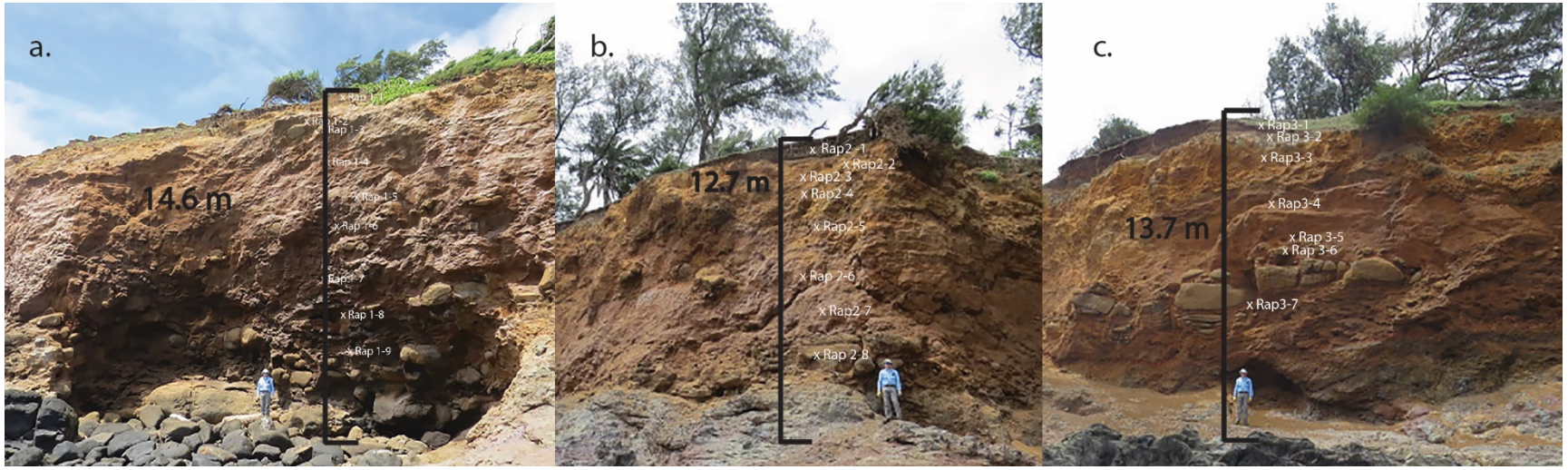

Figure 3: Photograph taken looking south west at the cliff-face. Sample locations and heights are recorded for Rap 1 (a), Rap 2 (b), and Rap 3(c). Samples were collected based on different physical properties, such as color, texture, and hardness. The "x" represents the actual location where the sample was collected. The three rappel locations have been adjusted so that the cliff faces are shown to scale.

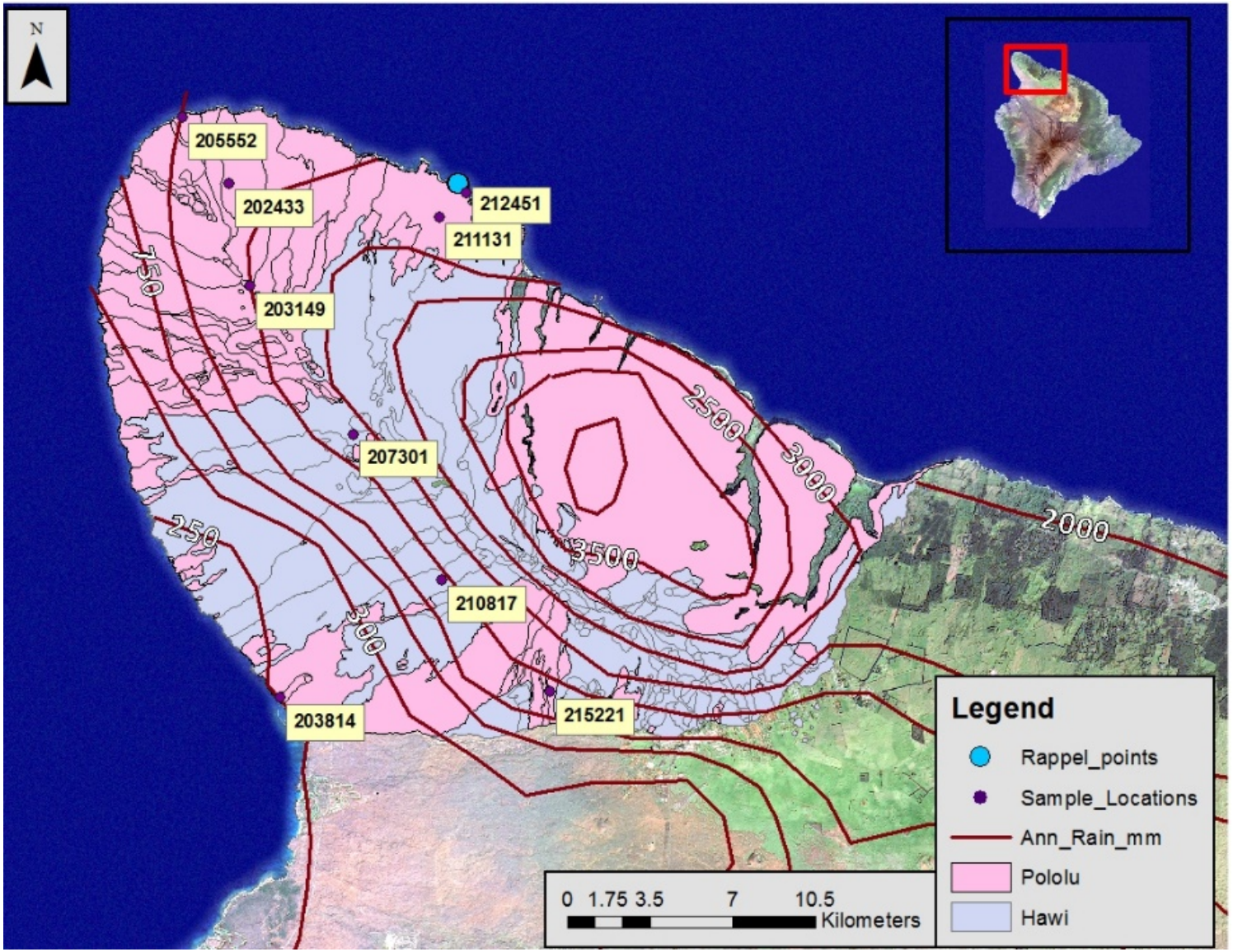

Figure 4: Map view of reconnaissance samples taken around the Kohala region, including annual rain in mm, as well as underlying flow units.

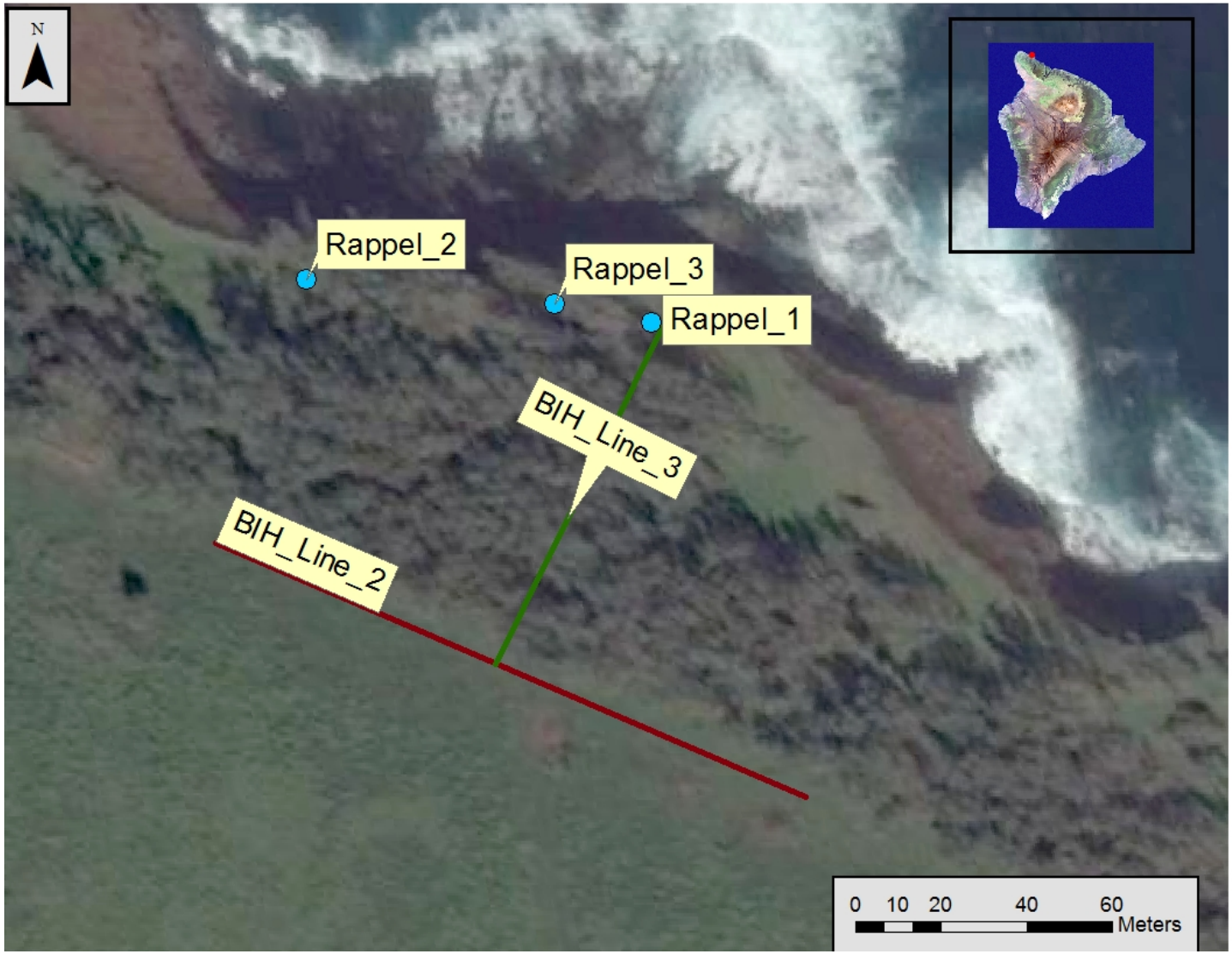

Figure 5: Location of two seismic survey lines for this study, BIH Line 2, and BIH Line 3 as well as Rappel points.

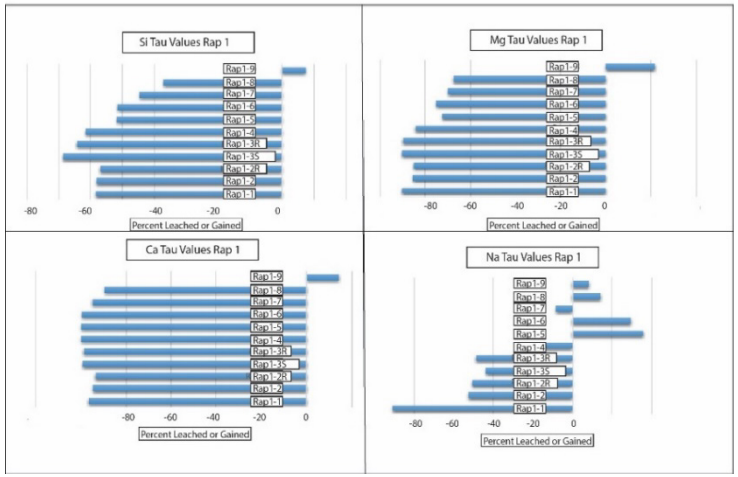

Figure 6: □ values of Si, Mg, Ca, and Na for Rappel 1. Generally, near-surface samples are extremely leached, and become less leached toward the bottom of the weathering profile. Exceptions include Rap 1-9 which contains smectite and gains of all elements Si, Mg, Ca, and Na.

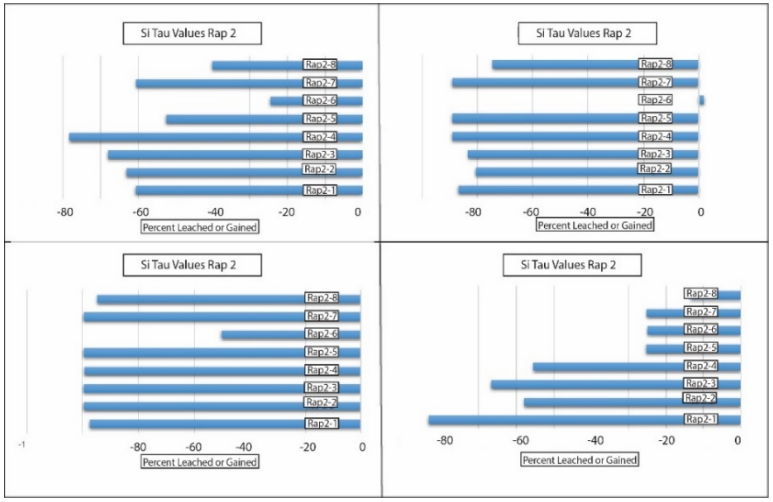

Figure 7: τ values of Si, Mg, Ca, and Na for Rappel 1. Generally, near-surface samples are extremely leached, and become less leached toward the bottom of the weathering profile. Exceptions include Rap 1-9 which contains smectite and gains of all elements Si, Mg, Ca, and Na.

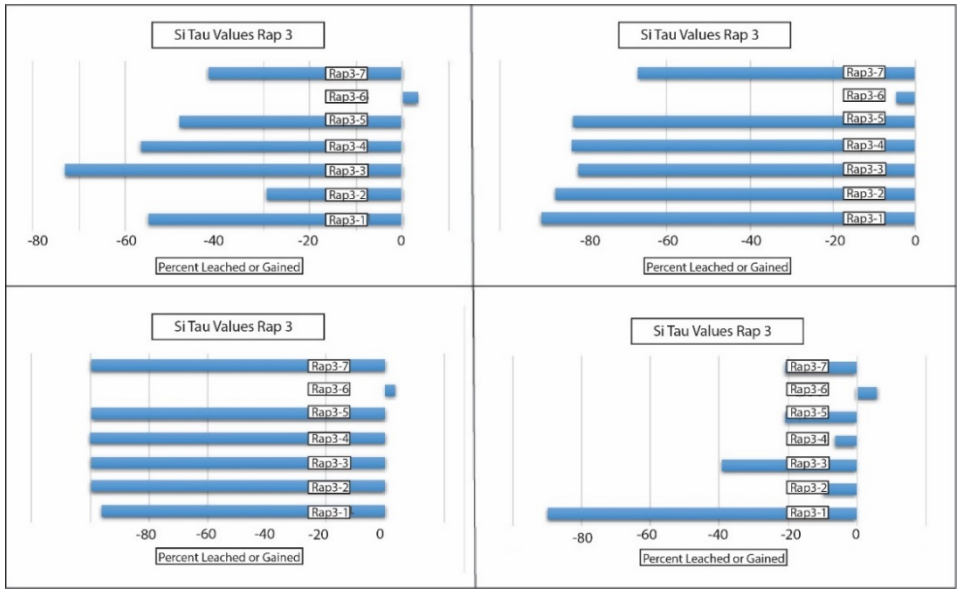

Figure 8: τ values of Si, Mg, Ca, and Na for Rappel 1. Generally, near-surface samples are extremely leached, and become less leached toward the bottom of the weathering profile. Exceptions include Rap 1-9 which contains smectite and gains of all elements Si, Mg, Ca, and Na.

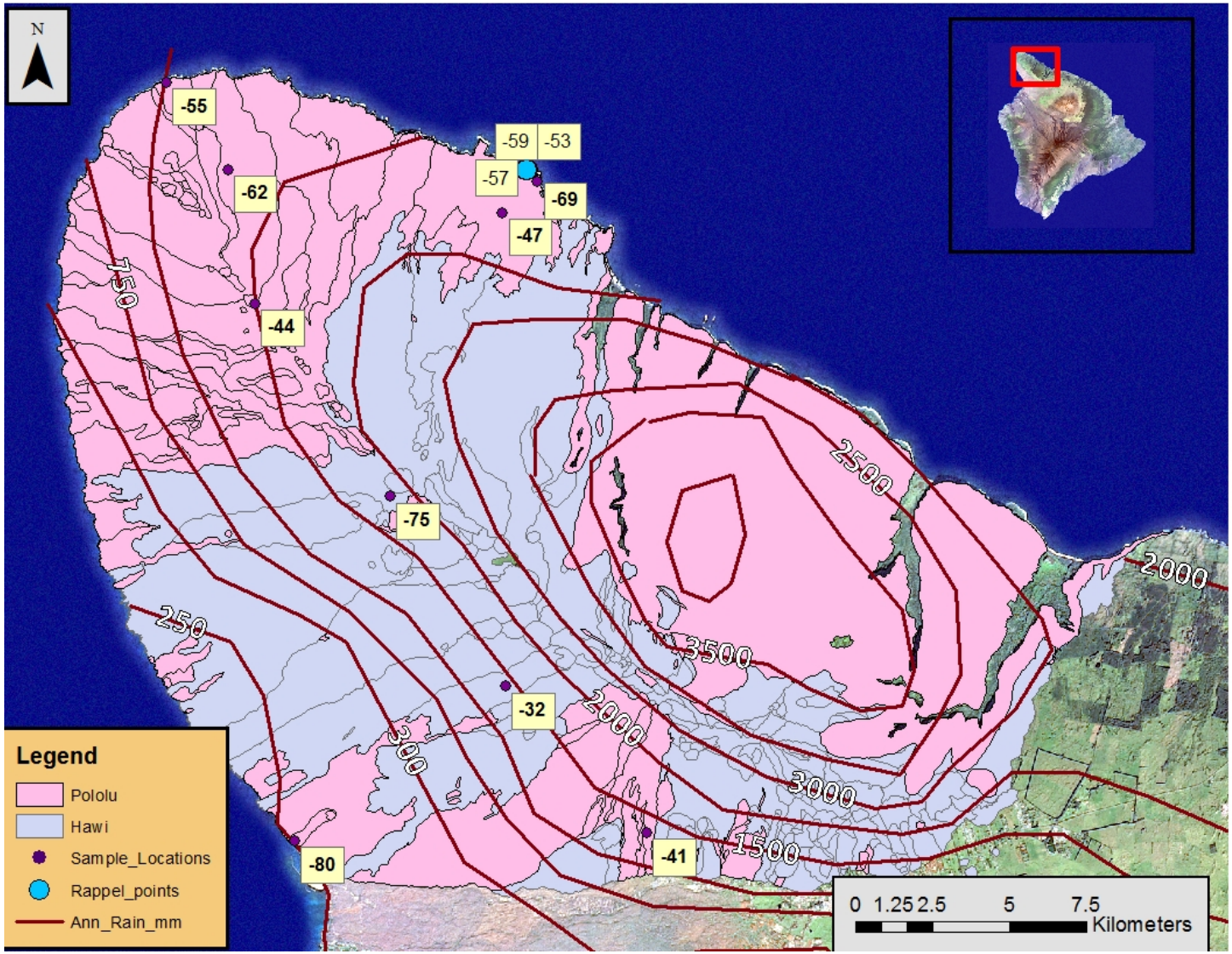

Figure: 9 Map view of surficial samples of Si τ values on the Kohala Peninsula. Although extensive weathering has occurred, the degree of weathering is not correlated with rainfall.

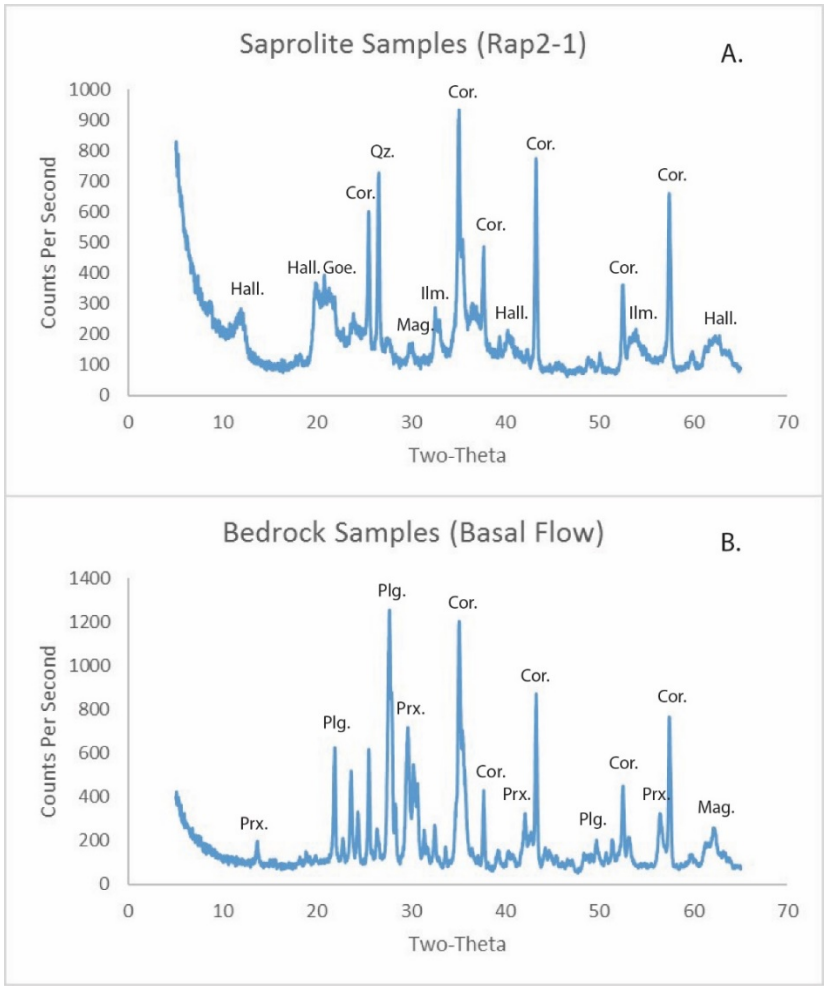

Figure 10: (s) X-ray diffraction pattern of a weathered saprolite. This pattern is representative of weathered samples. Around 12° two-theta (7- Å) a large peak for halloysite is present as well as peaks for Fe-Ti oxides, and gibbsite (b) X-ray diffraction pattern of a relatively unweathered sample taken at the base of the cliff-face. This pattern is representative of unweathered samples collected at this location. Peaks for fresh minerals such as anorthoclase, plagioclase, and pyroxene are present.

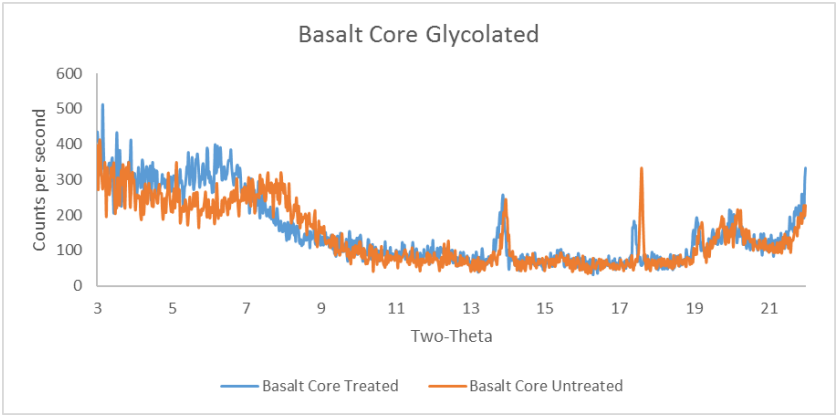

Figure 11: Representative pattern for a sample with smectite. Samples with smectites have a large flat peak around 8 two-theta. When glycolated, the treated sample shifts around 5 degrees two-theta.

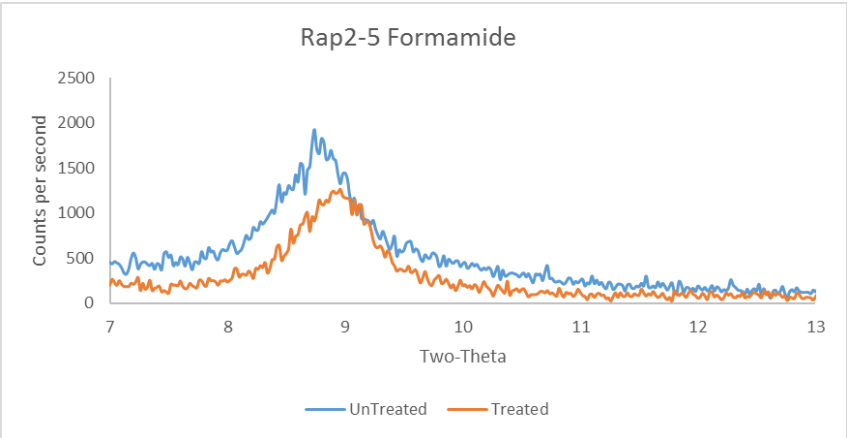

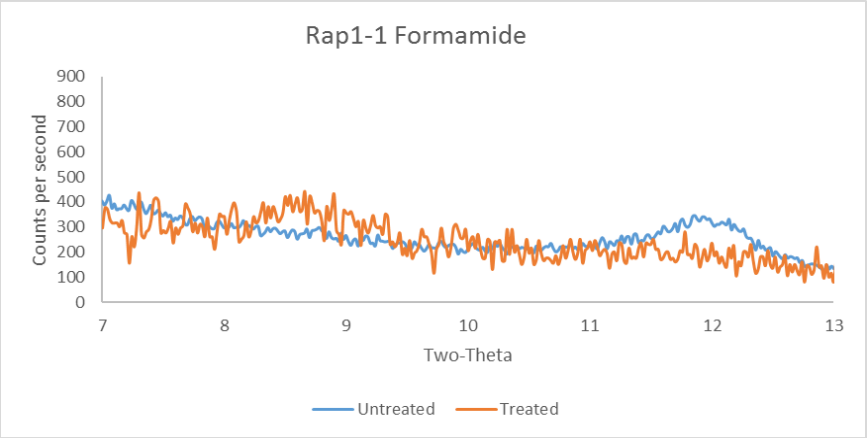

Figure 12: A) This pattern shows an untreated and formamide treated sample. Notice that there is no 12-degree peak, only an 8-degree peak as indicated for halloysite. After treatment only a small change in the peak is noted, because it is mostly composed of halloysite not kaolinite. B) This sample shows when the untreated sample was at the 12-degree peak and reacted with formamide. A majority of the peak shifted to the 8-degree peak. This sample contains a minimal amount of kaolinite as seen with a small peak at 12-degrees two theta.

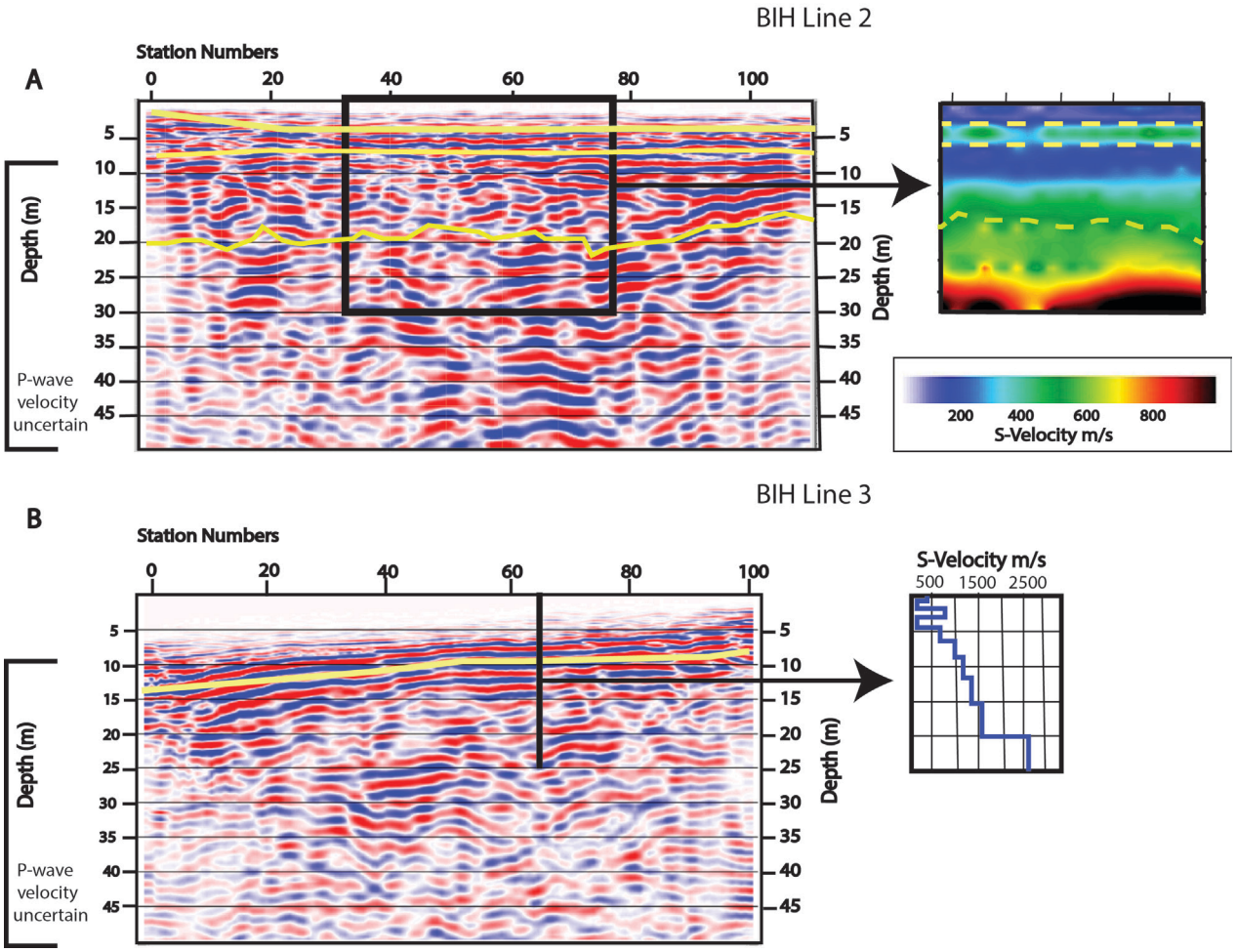

Figure 13: Geophysical stations represented are 1.52 m apart. Fresh basalt is defined at 500 m/s (Yaede et al., 2015). (a) Results of BIH Line 2, CDP survey with 2-D results of MASW survey. This line, while parallel to the cliff-face is perpendicular to past lava flows, and shows lenticular flow packages. Around 5 meters' depth a velocity inversion is present. Data below 5 meters' depth on the CDP is uncertain. (b) Results of BIH Line 3, CDP survey with 1-D results of MASW survey. BIH Line 3 shows reflectors dipping seaward parallel to the ground surface. The velocity inversion seen on BIH Line 2 is present in BIH Line 3 MASW results. However, no reflectors are present on the CDP until around 5 meters' depth. (c) Results of BIH Line 2 MASW passive-source survey. Velocities from the passive-source and active-source do not correlate until depth due to longer wavelengths of the passive survey.

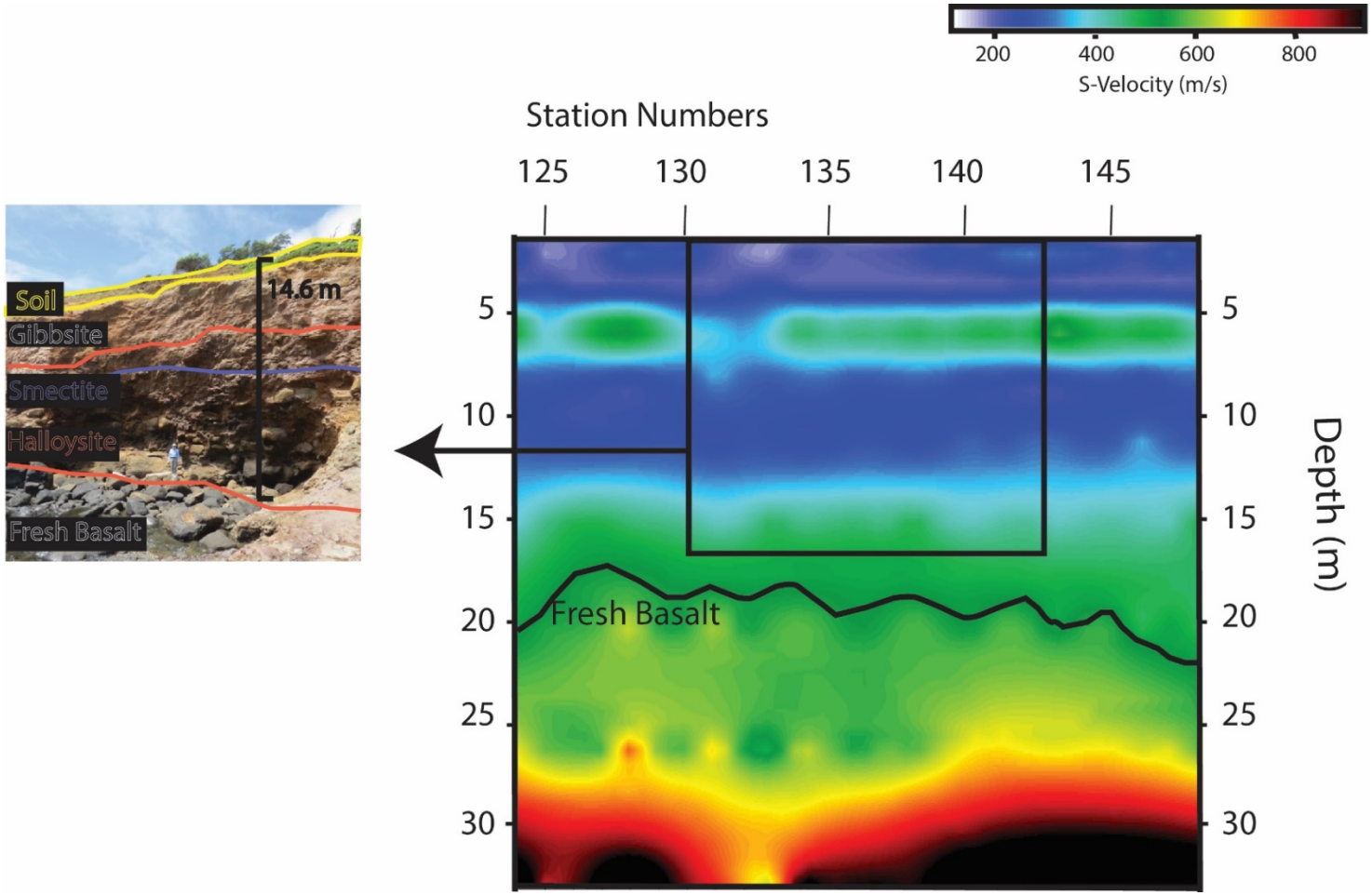

Figure 14: Horizon map showing horizons where gibbsite is favored at greater than 10 wt. %. The right side of the picture relates to the seismic profile, whereas the left side's scale is skewed due to an offset view. The ground surface at the top of the profile correlates to the depth 0 m on the MASW profile. This horizon matches the velocity inversion found on the seismic surveys. All samples that contained smectite were taken near this horizon where τ values are generally positive for Si, Ca, Mg, and Na.

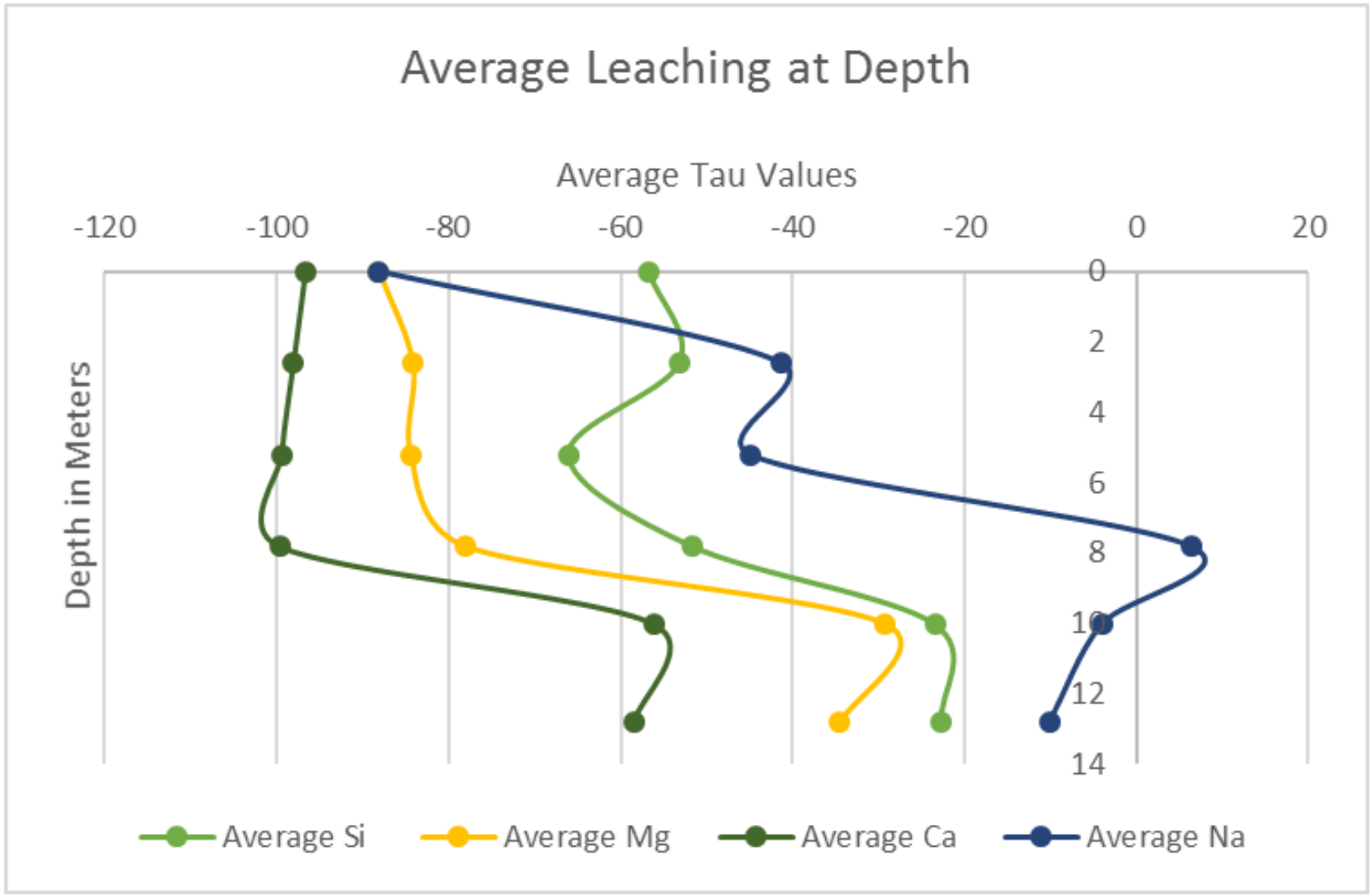

Figure 15: Si, Mg, Ca, and Na τ values as a function of depth. Samples located near the ground surface experienced more leaching than those at the base of the profile. Samples located right about 2 m depth show a relative silica gain compared to the surface. Samples located at 5 meters show a maximum silica leaching. Although smectite bearing samples contain positive tau values, they are the minority, and only slightly affect the average of all the samples.

APPENDIX 1

Table 1: XRD data for Rappel 1. R and S indicates a sample that was divided into rock (R) and soil (S) components.

Rappel 1 XRD Results											
Rap 1 Sample #	**1**	**2R**	**2S**	**3R**	**3S**	**4**	**5**	**6**	**7**	**8**	**9**
Degree of Fit	0.11	0.09	0.10	0.09	0.10	0.10	0.10	0.09	0.10	0.11	0.11
Non-Clays											
Quartz	3.4	0.0	0.2	0.0	0.0	0.0	0.0	0.0	0.0	0.0	0.0
Kspar	0.0	7.2	6.9	0.0	1.0	0.0	0.0	0.0	6.9	14.5	14.3
Plagioclase	0.0	0.0	0.0	0.0	0.0	0.0	0.0	0.0	0.0	0.0	28.4
Fe-Ti oxides	42.2	46.6	48.1	38.7	43.4	36.3	41.0	40.5	37.2	36.2	14.9
Halite	0.0	0.0	0.0	2.1	2.5	4.9	6.3	5.9	6.7	6.0	0.0
Forsterite	0.0	0.0	0.0	0.0	0.0	0.0	0.0	0.0	0.0	0.0	5.9
Analcime	0.0	0.0	0.0	0.0	0.0	0.0	0.0	0.0	0.0	0.0	0.0
Augite	0.0	0.0	0.0	0.0	0.0	0.0	0.0	0.0	0.0	0.0	23.4
Hypersthene	0.0	0.0	0.0	0.0	0.0	0.0	0.0	0.0	0.0	0.0	0.1
Diaspore	0.7	0.9	1.0	0.7	1.1	0.0	0.9	0.0	0.2	0.8	0.0
Total non-clays	46.3	54.7	56.1	41.6	48.1	41.2	48.1	46.4	51.0	57.5	87.0
Clays											
Halloysite	47.1	28.5	27.8	45.2	42.6	58.8	51.1	50.8	48.8	42.5	1.1
Kaolinite	2.1		0.0	0.0		0.0	0.0	2.0			
Gibbsite	4.5	16.8	16.0	13.2	9.3	0.0	0.8	0.8	0.2		0.0
Smectite	0.0	0.0	0.0	0.0	0.0	0.0	0.0	0.0	0.0	0.0	17.7
Total Clays	53.7	45.3	43.9	58.4	51.9	58.8	51.9	53.6	49.0	42.5	18.9
TOTAL	100.0	100.0	100.0	100.0	100.0	100.0	100.0	100.0	100.0	100.0	105.9

Table 2: XRD Data Rappel 2. R and S indicates a sample that was divided into rock (R) and soil (S) components.

Rappel 2 XRD Results								
Rap 2 Sample #	**1**	**2**	**3**	**4**	**5**	**6**	**7**	**8**
Degree of Fit	0.11	0.10	0.10	0.13	0.10	0.12	0.09	0.10
Non-Clays								
Quartz	6.8	0.1	0.0	0.0	0.0	0.0	0.0	0.0
Kspar	3.2	0.5	0.0	0.0	0.0	12.0	0.0	11.7
Plagioclase	0.0	0.0	0.0	0.0	0.0	0.0	0.0	0.0
Fe-Ti oxides	42.5	42.9	36.1	37.6	36.1	21.0	36.5	35.5
Halite	0.0	0.0	0.0	0.7	3.1	0.9	2.5	3.1
Forsterite	0.0	0.0	0.0	0.0	0.0	5.7	0.0	0.0
Analcime	0.0	0.0	0.0	0.0	0.0	16.5	0.0	0.0
Augite	0.0	0.0	0.0	0.0	0.0	0.2	0.0	0.0
Hypersthene	0.0	0.0	0.0	0.0	0.0	14.7	0.0	0.0
Diaspore	1.2	0.7	0.0	4.6	0.8	13.5	0.5	0.1
Total non-clays	53.7	44.2	36.1	42.9	39.9	84.5	39.5	50.3
Clays								
Halloysite	45.7	48.7	41.4	29.0	50.7	18.4	60.4	49.3
Kaolinite			0.0	0.0		0.0		
Gibbsite	0.6	7.1	22.5	28.1	9.4	2.7	0.1	0.4
Smectite	0.0	0.0	0.0	0.0	0.0	0.0	0.0	0.0
Total Clays	46.3	55.8	63.9	57.1	60.1	21.1	60.5	49.7
TOTAL	100.0	100.0	100.0	100.0	100.0	105.7	100.0	100.0

Table 3: XRD Data Rappel 3. R and S indicates a sample that was divided into rock (R) and soil (S) components.

Rappel 3 XRD Results							
Rap 3 Sample #	**1**	**2**	**3**	**4**	**5**	**6**	**7**
Degree of Fit	0.10	0.12	0.11	0.10	0.10	0.12	0.10
Non-Clays							
Quartz	3.6	0.0	0.1	0.0	0.0	0.0	0.0
Kspar	0.0	20.1	0.0	0.0	0.0	15.4	0.0
Plagioclase	0.0	0.0	0.0	0.0	0.0	29.9	0.0
Fe-Ti oxides	39.8	20.2	43.3	23.8	38.4	13.7	48.1
Halite	0.0	2.5	1.7	5.2	4.9	0.1	8.7
Forsterite	0.0	0.0	0.0	0.0	0.0	5.9	0.0
Analcime	0.0	0.0	0.0	0.0	0.0	0.0	0.0
Augite	0.0	0.0	0.0	0.0	0.0	28.3	0.0
Hypersthene	0.0	0.0	0.0	0.0	0.0	2.1	0.0
Diaspore	0.0	0.0	0.0	0.3	0.0	0.0	0.0
Total non-clays	43.4	42.9	45.1	29.3	43.3	95.2	56.8
Clays							
Halloysite	54.1	45.0	39.9	70.7	56.7	10.7	43.2
Kaolinite	0.1	0.0	0.0	0.0			0.0
Gibbsite	2.4	12.2	15.0		0.0	0.0	
Smectite	0.0	0.0	0.0	0.0	0.0	0.0	0.0
Total Clays	56.6	57.1	54.9	70.7	56.7	10.7	43.2
TOTAL	100.0	100.0	100.0	100.0	100.0	105.9	100.0

Table 4: XRD Data Miscellaneous samples.

Miscellaneous XRD Results										
	Misc. 1	Misc. 2	Misc. 3	Misc. 4	Misc. 5	Misc. 6	Misc. 7	Misc. 8	Misc. 9	Misc. 10
Degree of Fit	0.17	0.14	0.13	0.13	0.13	0.16	0.16	0.10	0.11	0.14
Non-Clays										
Quartz	0.0	0.0	0.0	0.0	0.0	0.0	0.0	0.3	0.0	0.0
Kspar	9.9	2.8	13.0	6.0	3.0	4.2	17.1	17.1	0.0	13.3
Plagioclase	50.0	55.0	31.5	17.9	26.4	52.3	35.9	0.0	0.0	22.0
Fe-Ti oxides	14.4	14.7	15.9	34.8	34.4	14.1	23.7	35.4	36.7	30.1
Halite	0.2	0.1	0.0	0.1	0.6	0.1	0.0	2.7	4.4	0.0
Forsterite	2.0	1.6	7.6	0.3	0.7	0.9	13.6	0.0	0.0	8.7
Analcime	0.0	0.0	0.0	0.0	0.0	0.0	0.0	0.0	0.0	0.0
Augite	22.0	17.6	22.4	15.7	17.5	20.2	23.2	0.0	0.0	27.5
Hypersthene	3.6	4.8	0.0	4.0	4.1	4.6	0.1	0.0	0.0	0.0
Diaspore	0.0	0.0	0.0	0.0	0.0	0.0	0.0	0.0	0.0	0.0
Total non-cla	102.0	96.6	90.5	78.9	86.7	96.4	113.6	55.5	41.1	101.6
Clays										
Halloysite	0.0	5.1	0.0	21.5	13.9	4.5	0.0	39.8	58.8	7.2
Kaolinite	0.0	0.0	0.0	0.0	0.0	0.0	0.0	4.6	0.0	0.0
Gibbsite	0.0	0.0	0.0	0.0	0.0	0.0	0.0	0.0	0.1	0.0
Smectite	0.0	0.0	17.2	0.0	0.0	0.0	0.0	0.0	0.0	0.0
Total Clays	0.0	5.1	17.2	21.5	13.9	4.5	0.0	44.5	58.9	7.2
TOTAL	102.0	101.7	107.6	100.3	100.6	100.9	113.6	100.0	100.0	108.7

Table 5: a) XRD data background samples.

Background XRD Results										
Misc.	**202433E**	**205552E**	**207301E**	**211131E**	**212451E**	**215221E**	**203149E**	**203814E**	**210817E**	**235477E**
Degree of Fit	0.10	0.11	0.10	0.09	0.11	0.09	0.09	0.11	0.15	0.11
Non-Clays										
Quartz	0.1	3.3	1.0	0.0	3.7	0.0	10.9	0.0	3.0	0.0
Kspar	0.0	0.0	0.0	0.0	0.0	0.0	0.0	0.0	0.0	17.5
Plagioclase	0.0	0.0	0.0	0.0	0.0	0.0	0.0	0.0	0.0	43.3
Fe-Ti oxides	51.0	35.4	98.8	32.1	29.5	39.9	45.4	56.8	97.0	25.5
Halite	0.0	0.0	0.0	0.0	0.0	0.0	0.0	0.0	0.0	0.0
Forsterite	0.0	0.0	0.0	0.0	0.0	0.0	0.0	0.0	0.0	0.0
Analcime	0.0	0.0	0.0	0.0	0.0	0.0	0.0	0.0	0.0	0.0
Augite	0.0	0.0	0.0	0.0	0.0	0.0	0.0	0.0	0.0	12.4
Hypersthene	0.0	0.0	0.0	0.0	0.0	0.0	0.0	0.0	0.0	0.0
Diaspore	0.0	0.0	0.0	0.0	0.0	0.0	0.0	0.0	0.0	0.0
Total non-clays	51.1	38.7	99.8	32.1	33.2	39.9	56.3	56.8	100.0	98.7
Clays										
Halloysite	30.0	57.1	0.0	64.6	65.3	60.1	39.2	36.9	0.0	0.0
Kaolinite	1.3	4.1	0.0	3.3	0.0	0.0	0.0	2.8	0.0	1.3
Gibbsite	17.5	0.0	0.0	0.0	1.5	0.0	4.6	3.5	0.0	0.0
Smectite	0.0	0.0	0.0	0.0	0.0	0.0	0.0	0.0	0.0	0.0
Total Clays	48.8	61.2	0.0	67.9	66.8	60.1	43.8	43.2	0.0	1.3
TOTAL	99.9	99.9	99.8	100.0	100.0	100.0	100.1	100.0	100.0	100.0

Table 6: Phenocryst data from MELTS. Two categories show the calculated weight percent and the chemical formula of the samples. Note that the remaining liquid does not have a chemical formula.

Phenocryst MELTS Results		
Name	**Mass %**	**Chemical Formula**
Liquid	85.36	
Olivine	3.63	$(Ca_1Mg_{74}Fe_{25}Mn_1)_2Si_{100}O_{400}$
Feldspar	9.61	$K_1Na_{36}Ca_{63}Al_{163}Si_{237}O_{800}$

Table 7: Matrix compositions from MELTS. Two categories show the calculated weight percent and the chemical formula of the samples. Note that this batch was allowed to crystalize to completion. Starting composition was calculated by subtracting composition of the phenocryst from the parent rock total formula.

Matrix MELTS Results		
Name	**Mass %**	**Chemical Formula**
Feldspar	42.78	$K_7Na_{50}Ca_{43}Al_{143}Si_{257}O_{800}$
Clinopyroxene	23.91	$Ca_{19}Fe_{89}Mg_{86}Fe_3Al_8Si_{194}O_{600}$
Clinopyroxene	20.14	$Na_2Ca_{79}Fe_{44}Mg_{65}Fe_5Ti_2Al_{13}Si_{190}O_{600}$
Spinel	4.16	$Fe_{141}Mg_{19}Fe_{71}Al_9Ti_{60}$
RHM-oxide	5.84	$Mn_4Fe_{79}Mg_7Fe_{18}Ti_{91}O_{300}$
Olivine	0.53	$(Ca_1Mg_{30}Fe_{56}Mn_{14})_2Si_{100}O_{400}$

Table 8: Major element totals normalized to 100% after LOIs have been added back in.

Major Elements Normalized to 100%												
Sample	**SiO_2**	**TiO_2**	**Al_2O_3**	**Fe_2O_3**	**MnO**	**MgO**	**CaO**	**Na_2O**	**K_2O**	**P_2O_5**	**LOI**	**Total**
200552E	31.5	5.0	24.2	20.9	0.6	0.9	0.4	0.5	0.8	0.6	14.6	100.0
202433E	23.2	4.4	33.2	18.8	0.3	0.6	0.1	0.0	0.1	0.6	18.6	100.0
203149E	28.5	3.7	24.1	17.4	0.4	1.1	0.4	0.1	1.3	0.8	22.3	100.0
203814E	17.6	6.3	28.7	27.3	0.2	0.9	0.2	0.1	0.4	0.3	18.0	100.0
207301E	17.1	4.9	28.1	19.1	0.3	2.9	0.5	0.0	0.1	2.9	24.3	100.0
210817E	30.7	3.2	16.7	14.0	0.2	2.4	4.5	2.0	0.8	1.9	23.7	100.0
211131E	30.0	4.0	26.7	20.6	0.1	0.5	0.1	1.4	0.1	0.4	15.9	100.0
212451E	27.4	6.3	25.0	22.8	0.2	1.0	0.3	0.4	0.7	0.7	15.2	100.0
215221E	35.4	4.2	25.0	17.8	0.3	2.6	1.3	0.2	0.1	0.5	12.7	100.0
235477E	44.1	3.0	17.2	13.7	0.2	4.1	7.0	2.7	1.3	0.7	5.8	100.0
Rap 1-1	30.6	5.1	22.9	22.5	0.3	1.1	0.5	0.3	0.6	0.6	15.5	100.0
Rap 1-2S	27.7	4.5	23.9	23.3	0.1	1.5	0.7	1.6	0.7	0.7	15.3	100.0
Rap 1-2R	27.3	4.4	24.2	22.9	0.2	1.5	0.8	1.6	0.6	0.6	15.9	100.0
Rap 1-3S	29.7	4.9	22.2	21.8	0.2	1.1	0.5	0.3	0.6	0.6	17.9	100.0
Rap 1-3R	24.9	4.8	24.6	23.4	0.1	1.1	0.2	2.5	0.4	0.5	17.5	100.0
Rap 1-4	25.0	4.5	20.8	23.8	0.2	1.5	0.1	4.0	0.4	0.4	19.4	100.0
Rap 1-5	26.5	3.8	18.8	20.8	0.3	2.3	0.1	5.5	0.6	0.4	21.1	100.0
Rap 1-6	27.7	3.9	18.9	20.7	0.2	2.1	0.1	5.4	1.0	0.4	19.5	100.0
Rap 1-7	31.1	3.9	18.7	19.7	0.2	2.6	0.7	4.4	1.1	0.4	17.3	100.0
Rap 1-8	32.8	3.6	17.6	17.9	0.2	2.6	1.2	4.7	1.3	0.5	17.4	100.0
Rap 1-9	45.2	2.9	13.5	15.0	0.2	7.7	9.6	2.4	0.9	0.4	2.3	100.0

Table 9: Major element totals normalized to 100% after LOIs have been added back in continued.

Major Elements Normalized to 100% Cont.												
Sample	**SiO_2**	**TiO_2**	**Al_2O_3**	**Fe_2O_3**	**MnO**	**MgO**	**CaO**	**Na_2O**	**K_2O**	**P_2O_5**	**LOI**	**Total**
Rap 2-1	29.5	5.2	20.1	22.4	0.3	1.5	0.4	0.6	0.8	0.5	18.8	100.0
Rap 2-2	25.0	4.7	25.1	23.3	0.1	2.0	0.0	1.5	0.3	0.5	17.7	100.0
Rap 2-3	21.1	4.5	27.3	23.9	0.2	1.6	0.0	1.1	0.2	0.6	19.5	100.0
Rap 2-4	15.2	4.8	30.1	25.2	0.1	1.1	0.1	1.8	0.2	0.6	20.9	100.0
Rap 2-5	24.6	3.6	25.8	19.0	0.3	0.8	0.1	2.8	0.3	0.4	22.4	100.0
Rap 2-6	35.5	3.2	17.9	16.9	0.2	7.2	4.7	2.2	0.5	0.4	11.3	100.0
Rap 2-7	27.5	4.8	22.7	21.9	0.5	1.1	0.1	3.3	0.3	0.3	17.5	100.0
Rap 2-8	36.0	4.1	19.8	19.5	0.2	2.3	0.7	3.6	1.2	0.5	12.1	100.0
Rap 3-1	30.8	4.7	21.4	20.6	0.3	1.0	0.5	0.4	0.6	0.7	19.1	100.0
Rap 3-2	28.6	2.8	37.0	5.9	0.0	0.8	0.0	2.5	0.3	0.1	22.0	100.0
Rap 3-3	18.3	4.6	26.5	24.1	0.1	1.9	0.1	2.6	0.3	0.5	21.1	100.0
Rap 3-4	27.4	4.3	24.3	14.6	0.1	1.7	0.1	4.4	0.5	0.2	22.4	100.0
Rap 3-5	30.7	4.1	20.2	21.7	0.2	1.6	0.1	3.8	0.7	0.5	16.3	100.0
Rap 3-6	43.8	2.9	14.0	16.3	0.1	6.1	8.7	2.3	0.8	0.4	4.4	100.0
Rap 3-7	31.4	3.7	18.4	21.0	0.2	2.7	0.1	4.7	1.1	0.5	16.3	100.0
Misc. 1	50.5	3.7	12.9	15.6	0.2	4.5	8.6	2.7	0.9	0.5	0.1	100.0
Misc. 2	44.4	2.7	12.9	14.4	0.2	10.2	10.0	2.0	0.7	0.3	2.2	100.0
Misc. 3	46.5	4.1	14.0	17.4	0.2	4.3	8.4	2.7	0.3	0.5	1.7	100.0
Misc. 4	39.5	4.4	15.4	18.9	0.2	3.7	4.9	2.4	0.3	0.5	9.8	100.0
Misc. 5	41.7	4.3	14.8	18.7	0.2	4.2	6.2	2.6	0.3	0.5	6.6	100.0
Misc. 6	46.3	3.9	13.6	17.6	0.2	4.4	8.7	2.9	0.3	0.5	1.5	100.0
Misc. 7	46.2	2.8	13.6	14.6	0.2	9.0	9.9	2.3	0.9	0.4	0.2	100.0
Misc. 8	30.8	3.4	17.2	16.8	0.3	2.9	1.6	2.7	0.9	0.4	22.9	100.0
Misc. 9	30.9	4.1	19.6	20.3	0.2	1.5	0.3	4.3	0.9	0.3	17.5	100.0
Misc. 10	43.1	2.7	13.3	15.8	0.2	8.0	8.5	2.1	0.8	0.4	5.2	100.0

Table 10: Major element totals normalized to 100% after sea water concentrations have been removed and LOIs have been added back in. Totals were recalculated to eliminate the effects of sea salts.

Major Elements Normalized to 100% LOIs Removing Seawater												
Sample	**SiO_2**	**TiO_2**	**Al_2O_3**	**Fe_2O_3**	**MnO**	**MgO**	**CaO**	**Na_2O**	**K_2O**	**P_2O_5**	**LOI**	**Total**
200552E	31.5	5.0	24.2	20.9	0.6	0.9	0.4	0.5	0.8	0.6	14.6	100.0
202433E	23.2	4.4	33.2	18.8	0.3	0.6	0.1	0.0	0.1	0.6	18.6	100.0
203149E	28.5	3.7	24.1	17.4	0.4	1.1	0.4	0.1	1.3	0.8	22.3	100.0
203814E	17.6	6.3	28.7	27.3	0.2	0.9	0.2	0.1	0.4	0.3	18.0	100.0
207301E	17.1	4.9	28.1	19.1	0.3	2.9	0.5	0.0	0.1	2.9	24.3	100.0
210817E	30.7	3.2	16.7	14.0	0.2	2.4	4.5	2.0	0.8	1.9	23.7	100.0
211131E	30.0	4.0	26.7	20.6	0.1	0.5	0.1	1.4	0.1	0.4	15.9	100.0
212451E	27.4	6.3	25.0	22.8	0.2	1.0	0.3	0.4	0.7	0.7	15.2	100.0
215221E	35.4	4.2	25.0	17.8	0.3	2.6	1.3	0.2	0.1	0.5	12.7	100.0
235477E	44.1	3.0	17.2	13.7	0.2	4.1	7.0	2.7	1.3	0.7	5.8	100.0
Rap 1-1	30.6	5.1	22.9	22.5	0.3	1.1	0.5	0.3	0.6	0.6	15.5	100.0
Rap 1-2S	27.7	4.5	23.9	23.3	0.1	1.5	0.7	1.6	0.7	0.7	15.3	100.0
Rap 1-2R	27.3	4.4	24.2	22.9	0.2	1.5	0.8	1.6	0.6	0.6	15.9	100.0
Rap 1-3S	23.7	5.2	22.4	26.1	0.1	1.2	0.1	2.2	0.5	0.6	17.9	100.0
Rap 1-3R	25.1	4.8	24.8	23.6	0.1	1.1	0.2	1.8	0.4	0.6	17.5	100.0
Rap 1-4	25.4	4.5	21.2	24.2	0.2	1.6	0.0	2.7	0.4	0.4	19.4	100.0
Rap 1-5	27.1	3.9	19.3	21.3	0.3	2.3	0.0	3.9	0.6	0.4	21.1	100.0
Rap 1-6	28.3	4.0	19.3	21.1	0.2	2.2	0.1	3.8	1.0	0.4	19.5	100.0
Rap 1-7	31.9	4.0	19.2	20.2	0.2	2.6	0.6	2.6	1.1	0.4	17.3	100.0
Rap 1-8	33.6	3.7	18.0	18.4	0.2	2.6	1.1	3.1	1.3	0.5	17.4	100.0
Rap 1-9	45.2	2.9	13.5	15.0	0.2	7.7	9.6	2.4	0.9	0.4	2.3	100.0

Table 10: Major element totals normalized to 100% after sea water concentrations have been removed and LOIs have been added back in. Totals were recalculated to eliminate the effects of sea salts cont.

Major Elements Normalized to 100% LOIs Removing Seawater Cont.												
Sample	**SiO_2**	**TiO_2**	**Al_2O_3**	**Fe_2O_3**	**MnO**	**MgO**	**CaO**	**Na_2O**	**K_2O**	**P_2O_5**	**LOI**	**Total**
Rap 2-1	29.5	5.2	20.1	22.4	0.3	1.5	0.4	0.6	0.8	0.5	18.8	100.0
Rap 2-2	25.0	4.7	25.1	23.3	0.1	2.0	0.0	1.5	0.3	0.5	17.7	100.0
Rap 2-3	21.1	4.5	27.3	23.9	0.2	1.6	0.0	1.1	0.2	0.6	19.5	100.0
Rap 2-4	15.2	4.8	30.2	25.2	0.1	1.1	0.1	1.6	0.2	0.6	20.9	100.0
Rap 2-5	24.9	3.6	26.0	19.2	0.3	0.8	0.0	2.0	0.3	0.4	22.4	100.0
Rap 2-6	35.7	3.2	18.0	16.9	0.2	7.2	4.7	1.9	0.5	0.4	11.3	100.0
Rap 2-7	27.7	4.8	22.9	22.1	0.5	1.1	0.0	2.7	0.2	0.3	17.5	100.0
Rap 2-8	36.4	4.2	20.1	19.7	0.2	2.3	0.6	2.7	1.1	0.5	12.1	100.0
Rap 3-1	30.8	4.7	21.4	20.6	0.3	1.0	0.5	0.4	0.6	0.7	19.1	100.0
Rap 3-2	28.9	2.8	37.3	5.9	0.0	0.8	0.0	1.9	0.2	0.1	22.0	100.0
Rap 3-3	18.4	4.7	26.7	24.2	0.1	1.9	0.0	2.1	0.3	0.5	21.1	100.0
Rap 3-4	27.9	4.4	24.8	14.8	0.1	1.7	0.0	3.1	0.5	0.2	22.4	100.0
Rap 3-5	31.3	4.1	20.5	22.1	0.2	1.6	0.1	2.5	0.7	0.6	16.3	100.0
Rap 3-6	43.9	2.9	14.0	16.3	0.1	6.1	8.7	2.3	0.8	0.4	4.4	100.0
Rap 3-7	32.4	3.8	19.0	21.7	0.2	2.8	0.0	2.3	1.0	0.5	16.3	100.0
Misc. 1	50.5	3.7	12.9	15.6	0.2	4.5	8.6	2.6	0.9	0.5	0.1	100.0
Misc. 2	44.5	2.7	12.9	14.4	0.2	10.2	10.0	2.0	0.7	0.3	2.2	100.0
Misc. 3	46.5	4.1	14.0	17.4	0.2	4.3	8.4	2.7	0.3	0.5	1.7	100.0
Misc. 4	39.5	4.4	15.4	18.9	0.2	3.7	4.9	2.4	0.3	0.5	9.8	100.0
Misc. 5	41.8	4.3	14.9	18.8	0.2	4.2	6.2	2.4	0.3	0.5	6.6	100.0
Misc. 6	46.3	3.9	13.6	17.6	0.2	4.4	8.7	2.9	0.3	0.5	1.5	100.0
Misc. 7	46.2	2.8	13.6	14.6	0.2	9.0	9.9	2.3	0.9	0.4	0.2	100.0
Misc. 8	31.1	3.4	17.4	17.0	0.3	2.9	1.6	2.0	0.9	0.4	22.9	100.0
Misc. 9	31.4	4.2	19.9	20.7	0.2	1.6	0.2	3.1	0.9	0.3	17.5	100.0
Misc. 10	43.1	2.7	13.3	15.8	0.2	8.0	8.5	2.1	0.8	0.4	5.2	100.0

Table 11: Trace element concentrations after LOI losses were added back in.

Normalized Trace Elements Including Sea Water																				
	Ba	Ce	Cr	Cu	Ga	La	Nb	Nd	Ni	Pb	Rb	Sc	Sm	Sr	Th	U	V	Y	Zn	Zr
200552E	209.4	67.3	168.4	92.4	24.3	35.7	28.5	39.2	82.1	9.7	21.9	25.4	5.2	51.7	4.6	2.3	349.6	39.5	195.7	257.2
202433E	53.3	25.9	162.1	92.5	34.0	0.0	37.5	25.4	82.2	3.3	2.9	36.6	9.1	31.3	3.6	1.5	585.2	12.6	131.3	350.2
203149E	200.5	74.6	156.5	85.8	26.1	49.8	39.2	42.7	71.6	13.1	43.3	12.8	5.1	108.6	7.6	3.0	239.4	46.3	173.8	278.5
203814E	89.8	63.4	301.2	140.0	44.4	52.3	51.1	46.8	105.3	10.9	28.0	25.3	6.4	86.0	4.9	1.6	590.3	45.4	154.1	373.6
211131E	113.3	43.0	735.9	97.3	25.2	15.6	20.7	23.3	321.2	2.1	0.3	38.3	4.0	8.4	0.2	0.6	425.7	5.4	94.3	202.4
212451E	78.6	50.5	413.0	81.5	31.6	26.4	42.3	25.6	182.0	10.7	19.6	27.4	4.4	38.1	5.0	1.9	434.0	19.7	115.7	344.0
235477E	437.1	70.4	49.0	28.0	18.3	37.8	36.0	40.9	23.2	4.2	27.0	15.0	5.0	765.7	3.5	0.0	119.9	35.2	128.7	301.5
207301E	32.9	219.6	16.7	3.2	19.4	62.5	62.8	90.8	5.8	5.3	2.1	10.3	18.9	41.6	6.8	2.6	121.9	39.5	117.4	606.7
210817E	322.6	88.4	45.7	19.6	18.6	51.0	46.6	55.5	10.7	16.6	18.6	11.8	6.2	801.8	2.4	0.0	84.2	49.0	245.2	292.6
215221E	223.8	121.9	232.6	38.9	26.5	33.0	32.9	69.2	161.5	4.6	3.1	60.0	13.7	149.0	3.9	1.7	326.9	31.7	93.9	385.7
Rap1-1	188.0	66.0	0.0	55.0	25.0	26.0	29.0	42.0	26.0	3.0	3.0	31.0	9.0	421.9	2.0	0.0	454.9	47.0	163.0	285.0
Rap1-2 R	172.8	67.9	0.0	70.9	27.0	24.0	33.0	41.0	33.0	5.0	4.0	31.0	11.0	179.8	2.0	0.0	460.6	48.0	185.8	324.7
Rap1-2 S	157.9	62.0	0.0	53.0	26.0	25.0	31.0	46.0	29.0	2.0	4.0	30.0	10.0	238.8	1.0	0.0	475.7	52.0	128.9	307.8
Rap1-3 R	206.0	71.0	0.0	56.0	24.0	24.0	28.0	37.0	25.0	3.0	4.0	30.0	9.0	431.9	1.0	0.0	457.9	44.0	150.0	281.0
Rap1-3 S	227.0	47.0	474.0	52.0	20.0	21.0	19.0	30.0	248.0	3.0	13.0	28.0	6.0	457.0	1.0	0.0	277.0	30.0	112.0	180.0
Rap1-4	162.7	78.9	808.7	104.8	38.9	22.0	50.9	49.9	313.5	13.0	28.0	39.9	13.0	70.9	6.0	2.0	660.0	33.9	231.6	444.3
Rap1-5	346.5	49.9	861.7	105.8	35.9	12.0	41.9	31.0	333.5	4.0	13.0	50.9	11.0	56.9	4.0	1.0	616.1	8.0	195.7	403.4
Rap1-6	284.5	51.9	859.6	107.8	35.9	12.0	39.9	33.9	334.5	5.0	11.0	51.9	12.0	58.9	3.0	1.0	608.0	8.0	197.7	399.4
Rap1-7	160.7	59.9	978.2	65.9	31.9	13.0	37.9	36.9	312.4	2.0	7.0	46.9	11.0	27.0	3.0	1.0	576.0	8.0	105.8	375.3
Rap1-8	447.2	63.9	668.8	59.9	22.0	30.9	23.0	54.9	232.6	2.0	18.0	36.9	10.0	167.7	2.0	1.0	343.4	39.9	85.8	228.6
Rap1-9	180.6	71.9	678.7	72.9	24.0	30.9	29.9	45.9	312.4	3.0	5.0	38.9	12.0	25.0	3.0	1.0	511.0	19.0	106.8	280.5
Rap2-1	213.5	68.9	686.6	51.9	22.0	54.9	25.9	105.8	272.4	2.0	6.0	41.9	14.0	34.9	2.0	1.0	454.0	78.8	49.9	252.5
Rap2-2	239.5	60.9	681.7	64.9	23.0	55.9	27.9	50.9	322.4	2.0	13.0	32.9	11.0	68.9	1.0	1.0	489.0	69.9	116.8	261.5
Rap2-3	141.8	55.9	618.9	63.9	23.0	26.0	28.0	47.9	245.6	1.0	16.0	34.9	11.0	125.8	1.0	1.0	429.3	42.9	70.9	270.5
Rap2-4	194.7	64.9	1199.9	78.9	34.9	11.0	42.9	36.9	321.4	3.0	8.0	53.9	11.0	30.9	3.0	2.0	642.9	10.0	113.8	418.3
Rap2-5	241.9	41.0	380.9	54.0	18.0	21.0	19.0	29.0	188.0	2.0	15.0	25.0	6.0	394.9	1.0	0.0	257.9	29.0	103.0	178.0
Rap2-6	186.6	73.9	1035.0	140.7	39.9	26.9	43.9	50.9	354.3	13.0	39.9	37.9	13.0	66.9	6.0	2.0	722.6	45.9	203.6	357.3
Rap2-7	19.0	34.9	1362.6	158.7	36.9	0.0	33.9	25.0	461.2	3.0	6.0	33.9	9.0	11.0	3.0	1.0	735.7	6.0	96.8	397.3
Rap2-8	15.0	16.0	1754.6	156.7	41.9	0.0	37.9	28.9	427.2	4.0	5.0	52.9	11.0	11.0	2.0	1.0	792.4	5.0	142.7	391.2
Rap3-1	90.8	10.0	1690.5	146.7	39.9	0.0	35.9	25.9	450.1	5.0	4.0	62.9	10.0	23.9	3.0	2.0	753.4	4.0	126.7	362.2
Rap3-2	174.6	95.8	1115.5	113.7	26.9	8.0	23.9	40.9	586.7	2.0	4.0	44.9	13.0	27.9	2.0	1.0	469.9	16.0	76.8	249.4
Rap3-3	176.8	22.0	981.9	103.9	24.0	9.0	22.0	34.0	474.5	1.0	6.0	35.0	7.0	103.9	0.0	0.0	422.5	26.0	150.8	222.7
Rap3-4	392.3	112.8	621.9	82.9	26.0	59.9	30.9	102.8	511.1	3.0	4.0	33.9	16.0	23.0	1.0	1.0	495.1	71.9	145.7	290.5
Rap3-5	222.7	60.9	679.2	78.9	25.0	29.0	28.0	52.9	272.7	2.0	18.0	34.0	10.0	109.9	1.0	0.0	398.5	41.0	149.8	267.7
Rap3-6	165.7	81.8	915.3	122.8	37.9	26.9	44.9	53.9	343.3	13.0	27.9	40.9	13.0	73.9	5.0	2.0	624.8	38.9	256.5	406.2
Rap3-7	19.0	14.0	766.3	60.9	21.0	0.0	18.0	13.0	514.9	4.0	5.0	14.0	4.0	22.0	5.0	2.0	253.4	3.0	65.9	243.5
Misc. 1	0.0	0.0	0.0	0.0	0.0	0.0	0.0	0.0	0.0	0.0	0.0	0.0	0.0	0.0	0.0	0.0	0.0	0.0	0.0	0.0
Misc. 2	0.0	0.0	0.0	0.0	0.0	0.0	0.0	0.0	0.0	0.0	0.0	0.0	0.0	0.0	0.0	0.0	0.0	0.0	0.0	0.0
Misc. 3	0.0	0.0	0.0	0.0	0.0	0.0	0.0	0.0	0.0	0.0	0.0	0.0	0.0	0.0	0.0	0.0	0.0	0.0	0.0	0.0
Misc. 4	0.0	0.0	0.0	0.0	0.0	0.0	0.0	0.0	0.0	0.0	0.0	0.0	0.0	0.0	0.0	0.0	0.0	0.0	0.0	0.0
Misc. 5	0.0	0.0	0.0	0.0	0.0	0.0	0.0	0.0	0.0	0.0	0.0	0.0	0.0	0.0	0.0	0.0	0.0	0.0	0.0	0.0
Misc. 6	227.0	58.0	0.0	60.0	21.0	23.0	24.0	29.0	24.0	3.0	16.0	26.0	7.0	370.0	1.0	0.0	398.0	39.0	143.0	236.0
Misc. 7	213.0	40.0	364.9	55.0	17.0	25.0	18.0	33.0	195.0	2.0	16.0	22.0	6.0	392.9	1.0	0.0	247.9	49.0	124.0	165.0
Misc. 8	87.8	28.9	1478.9	131.7	37.9	0.0	33.9	24.9	414.1	4.0	6.0	47.9	9.0	24.9	3.0	1.0	732.5	5.0	136.7	355.3
Misc. 9	297.3	73.8	650.5	37.9	30.9	6.0	33.9	26.9	523.8	3.0	7.0	34.9	9.0	41.9	3.0	2.0	489.9	11.0	69.8	306.3
Misc. 10	465.2	44.9	756.8	73.9	24.0	72.9	26.0	97.8	274.6	2.0	10.0	35.9	12.0	37.9	0.0	0.0	443.3	103.8	176.7	245.6

Table 12: Trace element concentrations after LOI losses were added back in. This shows corrected dilutions after sea water was removed.

Normalized ME No Seawater																				
Sample	**Ba**	**Ce**	**Cr**	**Cu**	**Ga**	**La**	**Nb**	**Nd**	**Ni**	**Pb**	**Rb**	**Sc**	**Sm**	**Sr**	**Th**	**U**	**V**	**Y**	**Zn**	**Zr**
200552E	263.9	76.0	175.9	91.4	23.9	29.9	29.9	47.8	88.0	8.5	23.9	25.6	10.2	52.9	4.3	1.7	385.1	41.0	204.1	277.5
202433E	52.9	26.1	162.0	92.8	34.2	0.0	37.5	25.2	82.2	3.3	3.3	36.6	9.0	30.9	3.3	1.6	585.5	13.0	131.1	350.1
203149E	240.2	86.3	165.6	84.7	25.7	56.8	41.2	56.8	77.8	13.2	44.3	13.2	10.1	109.6	7.8	2.3	267.5	46.7	182.7	300.1
203814E	164.0	74.6	317.3	141.9	44.3	39.4	54.9	59.9	124.6	13.1	30.3	25.4	13.1	89.4	5.7	1.6	655.2	47.6	161.5	415.7
207301E	33.3	219.6	16.7	3.0	19.7	62.8	62.8	90.9	6.1	5.3	2.3	10.6	18.9	41.6	6.8	2.3	121.9	39.4	117.4	606.4
210817E	357.8	118.3	44.3	19.8	18.3	55.7	47.3	78.6	16.0	16.8	17.5	10.7	12.2	789.7	3.8	0.0	105.3	49.6	254.1	296.8
211131E	168.2	37.8	789.5	96.7	24.4	0.8	21.0	21.0	334.6	2.5	1.7	38.7	8.4	8.4	1.7	0.8	465.0	5.9	96.7	221.1
212451E	144.1	64.4	443.3	81.4	31.4	16.1	44.9	27.1	192.4	11.0	21.2	27.1	9.3	39.0	5.1	1.7	482.3	17.8	119.5	374.7
215221E	223.5	122.2	232.3	39.3	26.2	33.2	33.2	69.0	161.5	4.4	3.5	60.3	14.0	149.3	4.4	1.7	326.6	31.4	94.3	386.0
235477E	464.6	99.9	48.1	28.3	18.8	39.6	36.7	49.9	25.4	3.8	27.3	15.1	9.4	765.1	2.8	0.0	133.8	34.9	131.9	307.2
Rap1-1	137.5	66.7	683.4	88.6	32.9	18.6	43.0	42.2	264.9	11.0	23.6	33.7	11.0	59.9	5.1	1.7	557.7	28.7	195.7	375.4
Rap1-2R	293.4	42.3	729.7	89.6	30.4	10.1	35.5	26.2	282.4	3.4	11.0	43.1	9.3	48.2	3.4	0.8	521.7	6.8	165.7	341.6
Rap1-2 S	239.3	43.7	723.0	90.7	30.2	10.1	33.6	28.6	281.3	4.2	9.2	43.7	10.1	49.5	2.5	0.8	511.4	6.7	166.3	335.9
Rap1-3R	131.9	49.2	802.9	54.1	26.2	10.7	31.1	30.3	256.4	1.6	5.7	38.5	9.0	22.1	2.5	0.8	472.7	6.6	86.8	308.1
Rap1-3S	369.0	52.7	551.8	49.4	18.1	25.5	18.9	45.3	191.9	1.6	14.8	30.5	8.2	138.4	1.6	0.8	283.3	32.9	70.8	188.6
Rap1-4	145.5	57.9	546.7	58.7	19.3	24.9	24.1	37.0	251.7	2.4	4.0	31.4	9.6	20.1	2.4	0.8	411.7	15.3	86.0	225.9
Rap1-5	168.6	54.4	542.0	41.0	17.3	43.3	20.5	83.5	215.1	1.6	4.7	33.1	11.0	27.6	1.6	0.8	358.4	62.2	39.4	199.3
Rap1-6	192.9	49.0	548.9	52.2	18.5	45.0	22.5	41.0	259.6	1.6	10.4	26.5	8.8	55.5	0.8	0.8	393.8	56.3	94.0	210.6
Rap1-7	117.3	46.3	512.2	52.9	19.0	21.5	23.1	39.7	203.2	0.8	13.2	28.9	9.1	104.1	0.8	0.8	355.2	35.5	58.7	223.9
Rap1-8	160.7	53.6	990.6	65.1	28.8	9.1	35.4	30.5	265.4	2.5	6.6	44.5	9.1	25.5	2.5	1.6	530.8	8.2	94.0	345.3
Rap1-9	236.3	40.0	372.0	52.7	17.6	20.5	18.6	28.3	183.6	2.0	14.6	24.4	5.9	385.7	1.0	0.0	251.9	28.3	100.6	173.8
Rap2-1	151.5	60.0	840.3	114.2	32.4	21.9	35.7	41.3	287.6	10.5	32.4	30.8	10.5	54.3	4.9	1.6	586.6	37.3	165.3	290.1
Rap2-2	15.6	28.8	1121.5	130.6	30.4	0.0	27.9	20.5	379.6	2.5	4.9	27.9	7.4	9.0	2.5	0.8	605.6	4.9	79.7	327.0
Rap2-3	12.0	12.9	1411.9	126.1	33.7	0.0	30.5	23.3	343.7	3.2	4.0	42.6	8.8	8.8	1.6	0.8	637.7	4.0	114.8	314.8
Rap2-4	71.8	7.9	1337.0	116.0	31.6	0.0	28.4	20.5	356.0	3.9	3.2	49.7	7.9	18.9	2.4	1.6	595.9	3.2	100.2	286.5
Rap2-5	135.6	74.4	866.2	88.3	20.9	6.2	18.6	31.8	455.6	1.5	3.1	34.9	10.1	21.7	1.5	0.8	364.9	12.4	59.7	193.7
Rap2-6	156.9	19.5	871.2	92.2	21.3	8.0	19.5	30.1	421.0	0.9	5.3	31.0	6.2	92.2	0.0	0.0	374.9	23.0	133.8	197.6
Rap2-7	323.5	93.0	512.8	68.3	21.4	49.4	25.5	84.8	421.5	2.5	3.3	28.0	13.2	18.9	0.8	0.8	408.3	59.3	120.2	239.5
Rap2-8	195.7	53.5	596.8	69.3	21.9	25.5	24.6	46.5	239.6	1.8	15.8	29.8	8.8	96.5	0.9	0.0	350.2	36.0	131.6	235.2
Rap3-1	134.1	66.2	740.7	99.4	30.7	21.8	36.3	43.6	277.9	10.5	22.6	33.1	10.5	59.8	4.0	1.6	505.7	31.5	207.6	328.8
Rap3-2	14.8	10.9	597.5	47.5	16.3	0.0	14.0	10.1	401.4	3.1	3.9	10.9	3.1	17.1	3.9	1.6	197.6	2.3	51.3	189.8
Rap3-3	69.3	22.8	1167.4	104.0	29.9	0.0	26.8	19.7	326.9	3.2	4.7	37.8	7.1	19.7	2.4	0.8	578.2	3.9	107.9	280.4
Rap3-4	230.8	57.3	505.1	29.4	24.0	4.6	26.3	20.9	406.7	2.3	5.4	27.1	7.0	32.5	2.3	1.5	380.4	8.5	54.2	237.8
Rap3-5	389.3	37.6	633.2	61.8	20.0	61.0	21.7	81.9	229.7	1.7	8.4	30.1	10.0	31.7	0.0	0.0	370.9	86.9	147.9	205.5
Rap3-6	257.9	36.3	486.2	55.4	18.2	32.5	19.1	37.3	352.5	1.9	13.4	25.8	6.7	330.5	1.0	0.0	280.9	47.8	179.6	179.6
Rap3-7	218.2	45.2	517.6	54.3	15.9	15.9	20.1	36.8	229.1	1.7	11.7	24.2	8.4	52.7	0.8	0.8	345.3	31.8	56.0	188.1
Misc. 1	226.9	58.0	0.0	60.0	21.0	23.0	24.0	29.0	24.0	3.0	16.0	26.0	7.0	369.8	1.0	0.0	397.8	39.0	142.9	235.9
Misc. 2	208.2	39.1	356.8	53.8	16.6	24.4	17.6	32.3	190.6	2.0	15.6	21.5	5.9	384.2	1.0	0.0	242.4	47.9	121.2	161.3
Misc. 3	184.7	64.9	0.0	54.0	24.6	25.6	28.5	41.3	25.6	2.9	2.9	30.5	8.8	414.7	2.0	0.0	447.1	46.2	160.2	280.1
Misc. 4	156.1	61.4	0.0	64.1	24.4	21.7	29.8	37.0	29.8	4.5	3.6	28.0	9.9	162.5	1.8	0.0	416.1	43.3	167.9	293.3
Misc. 5	147.6	57.9	0.0	49.5	24.3	23.4	29.0	43.0	27.1	1.9	3.7	28.0	9.3	223.2	0.9	0.0	444.6	48.6	120.5	287.7
Misc. 6	203.0	70.0	0.0	55.2	23.6	23.6	27.6	36.5	24.6	3.0	3.9	29.6	8.9	425.7	1.0	0.0	451.3	43.4	147.8	276.9
Misc. 7	226.6	46.9	473.2	51.9	20.0	21.0	19.0	29.9	247.6	3.0	13.0	28.0	6.0	456.2	1.0	0.0	276.5	29.9	111.8	179.7
Misc. 8	166.1	49.2	408.2	56.9	19.2	16.9	17.7	33.8	203.7	1.5	13.8	26.1	7.7	104.6	1.5	0.8	292.2	27.7	118.4	176.8
Misc. 9	85.7	35.4	522.2	58.5	17.3	16.5	19.8	32.9	180.4	2.5	8.2	22.2	8.2	48.6	1.6	0.8	295.7	28.0	103.0	184.5
Misc. 10	256.8	28.4	453.0	49.3	14.2	16.1	15.2	25.6	284.3	1.9	11.4	18.0	5.7	254.0	0.0	0.0	188.6	22.7	121.3	140.3

Table 13: τ values for background Kohala samples and hard rock samples collected at the base of the cliff. Values represent net gain (positive) values and need leached (negative) values. Colors have been added for a visual effect. Highlighted terms show samples that contain smectites.

Tau										
Sample	**SiO_2**	**TiO_2**	**Al_2O_3**	**Fe_2O_3**	**MnO**	**MgO**	**CaO**	**Na_2O**	**K_2O**	**P_2O_5**
200552E	-55	0	18	-13	110	-91	-97	-86	-21	-4
202433E	-63	0	83	-12	22	-93	-99	-99	-86	8
203149E	-45	0	59	-2	104	-85	-96	-98	82	59
203814E	-80	0	10	-10	-31	-93	-99	-97	-69	-66
207301E	-75	0	40	-19	8	-71	-96	-100	-94	357
210817E	-32	0	27	-9	39	-63	-49	-18	23	341
211131E	-47	0	60	6	-34	-94	-99	-53	-93	-22
212451E	-69	0	-3	-25	-43	-92	-98	-92	-47	-14
215221E	-41	0	43	-13	17	-70	-89	-94	-88	-17
235477E	3	0	37	-7	40	-32	-17	16	118	83
Misc. 1	-4	0	-16	-13	2	-40	-17	-6	18	-2
Misc. 2	18	0	18	12	33	90	34	-2	23	0
Misc. 3	-19	0	-16	-11	-17	-48	-26	-12	-66	-3
Misc. 4	-37	0	-16	-12	-11	-58	-61	-29	-65	-23
Misc. 5	-31	0	-16	-9	-20	-52	-48	-27	-66	-10
Misc. 6	-16	0	-15	-7	14	-44	-20	-2	-67	-1
Misc. 7	17	0	18	8	3	60	27	7	53	0
Misc. 8	-36	0	22	2	64	-58	-83	-21	32	-19
Misc. 9	-46	0	16	3	-7	-81	-98	0	9	-46
Misc. 10	12	0	18	20	1	46	11	3	43	8

Table 14: τ values represent net gain (positive) values and need leached (negative) values. Colors have been added for a visual effect. Highlighted terms show samples that contain smectites.

Tau Cont.										
Sample	SiO_2	TiO_2	Al_2O_3	Fe_2O_3	MnO	MgO	CaO	Na_2O	K_2O	P_2O_5
Rap 1-1	-57	0	10	-8	-9	-89	-96	-91	-41	-2
Rap 1-2S	-57	0	28	6	-42	-84	-94	-53	-27	9
Rap 1-2R	-56	0	34	8	-29	-83	-93	-51	-35	10
Rap 1-3S	-68	0	5	4	-55	-89	-99	-45	-48	-11
Rap 1-3R	-63	0	24	1	-53	-89	-99	-50	-60	-13
Rap 1-4	-60	0	13	10	-31	-83	-100	-22	-60	-29
Rap 1-5	-50	0	21	14	26	-70	-100	33	-28	-24
Rap 1-6	-50	0	17	9	2	-73	-99	25	23	-16
Rap 1-7	-43	0	17	5	-21	-67	-95	-12	36	-21
Rap 1-8	-35	0	19	3	10	-64	-89	13	71	11
Rap 1-9	11	0	13	7	-3	32	19	8	51	-1
Rap 2-1	-59	0	-5	-10	-2	-86	-97	-84	-23	-34
Rap 2-2	-62	0	31	3	-61	-79	-100	-58	-72	-24
Rap 2-3	-67	0	47	9	-32	-82	-100	-67	-82	-7
Rap 2-4	-77	0	53	9	-60	-88	-100	-56	-82	-12
Rap 2-5	-51	0	75	10	56	-88	-100	-25	-64	-10
Rap 2-6	-22	0	34	8	-10	11	-48	-21	-30	-10
Rap 2-7	-59	0	15	-5	98	-88	-100	-26	-76	-47
Rap 2-8	-38	0	16	-3	-11	-72	-95	-16	36	-3
Rap 3-1	-54	0	10	-9	16	-89	-96	-90	-36	7
Rap 3-2	-27	0	222	-56	-85	-86	-100	-11	-57	-81
Rap 3-3	-72	0	38	7	-59	-80	-100	-40	-72	-18
Rap 3-4	-55	0	36	-31	-39	-81	-100	-7	-43	-72
Rap 3-5	-47	0	20	10	1	-81	-100	-20	-16	2
Rap 3-6	7	0	16	16	-17	4	7	5	38	7
Rap 3-7	-40	0	19	16	-9	-64	-100	-23	31	-7